University of Alberta

Triggering on Single Top Events at the DØ Experiment

by

Master's Thesis by Kevin Chan

A thesis submitted to the Faculty of Graduate Studies and Research in partial fulfillment of the requirements for the degree of **Master of Science**.

Department of Physics

Edmonton, Alberta

Abstract

Data, collected at the DØ Detector using the online trigger list from version 8 to version 14, is used to calculate a combination of triggers useful in top quark searches. The single electron and electron + jets triggers were then folded into Monte-Carlo created single top signal events to create a logical OR of the triggers. These are then compared to the original pre-combination triggers to determine the amount of efficiency gained for the triggers.

Contents

1 Theory **3**

1.1 The Standard Model 3

1.2 The Single Top Quark 8

2 The DØ Detector **12**

2.1 An Overview of the Detector 12

2.2 The Tracking System 14

2.3 The Calorimeters 19

2.4 The Muon System 21

2.5 The Trigger 23

2.5.1 Level 1 trigger 24

2.5.2 Level 2 trigger 25

2.5.3 Level 3 trigger 27

3 Caf Trigger **29**

3.1 Purpose 29

3.2 Design and Implementation 31

3.2.1 Probability Processor 32

3.2.2 The Output Processor 34

4 Electron Trigger "OR'ing" **36**

4.1 Triggers of interest and "OR'ing" 36

4.2 The Turn-on Curves 45

4.3 Trigger Efficiencies in caf_trigger 51

4.3.1 The Single Electron, and e+Jets Triggers 51
4.3.2 "OR'ing" and Results 54

5 Conclusions **59**

Introduction

The top quark was discovered in 1995 by two collaborations at the Fermi National Accelerator Laboratory in 1995, at a high energy $p\bar{p}$ collider known as the Tevatron. This discovery involved searching for a top quark pair that was produced in the collisions. The current search involving the top quark is for the production of a single top quark, which is the only quark known to decay into its constituents without undergoing a process known as hadronization. This makes the single top an important observation for reasons that will be covered in the following chapters. The first chapter will describe the theory behind the Standard Model of particle physics, the top quark, and the characteristics of how a top quark decays.

The second chapter is an overview of the DØ Detector, which is situated at a location on the ring of the Tevatron at a site known as DØ. The Tevatron was completed in 1983 and has collected analysis quality data since 1988, and completed an upgrade in 1998. The upgraded Tevatron increased its centre of mass energy of the collision from $\sqrt{s} = 1.8$ TeV to $\sqrt{s} = 1.96$ TeV. Two particle detectors were commissioned at the Tevatron, the CDF detector and the DØdetector [1]. The DØ Detector was also upgraded to account for the increased rate of collisions supplied by the Tevatron. A short history, and an accounting of the upgraded systems will be covered.

The third chapter describes $caf_trigger$, a trigger efficiency tool created for the purpose of studying the efficiency of triggers used in detector. The triggers are the algorithms that make decisions on whether a given collision is interesting, based on the information detected, and stores this information if it is accepted. $caf_trigger$ allows for the study of these triggers by using data events that have passed or failed a

trigger, which have been derived from unbiased data. It then folds these efficiencies into offline simulated events (Monte-Carlo) to give a final trigger weight, which is the probability that an event has or has not passed a given trigger.

The fourth chapter is a trigger study of the triggers used in the analysis for the single top quark. Triggers are important in isolating groups of events which may contain the signal of an interesting occurance. The top quark (t-quark) is one such particle that requires the triggers chosen to be efficient in rejecting the background and keeping the signal. The triggers used are the single electron triggers and the electron + jets triggers. The logical ORs of the single electron triggers and the logical ORs of the electron + jets triggers will be produced. The *caf_trigger* package will then be used to study the combination, through logical ORs, of these triggers as a possible improvement of the triggers that have been used to collect the data. The goal of this is to judge whether there is a significant gain in the efficiency of the trigger combination, single electron ORs or electron + jets ORs.

Chapter 1

Theory

1.1 The Standard Model

Our current theories on particle physics began its developement in Einstein's theory of the photoelectric effect in 1905, which gave the first insights into the wave-particle duality of particles. This was further developed by de Broglie in 1923 [2] to describe all material particles in terms of waves as photons had been. During the 1930s, H. Yukawa proposed the meson as the mediator of the strong force, W. Pauli proposed the existence of the neutrino leading to the theory of the weak force and Carl Anderson found evidence of the anti-electron (positron). During this time, many physicists were laying the foundation of the quantum mechanics of these particles. Many particles were found over the course of the years including with the strangest being the aptly named "strange" particle, discovered by G. D. Rochester and C. C. Butler which introduced the quantum number "strange". These particles could be grouped together, conserved charge and strangeness, and had other bewildering properties. The baryons and mesons, with their charge and strange quantum numbers, were then organized into geometric groupings called the Eightfold Way by Murray Gell-Mann in 1961 [3]. This lead to the idea of quarks by Gell-Mann in 1964 as the elementary constituents of the baryons and mesons. This would group the elementary particles into leptons, like the electron and the neutrino, and quarks which made up the baryons and mesons. Over the years, more particles would be found and a few more quantum numbers such as quark colour and the mediators of the weak force, the intermediate vector bosons. These would lead up to what is

now known as the Standard Model (SM).

The Standard Model is the current understood theory which describes the 3 of the 4 fundamental forces of physics. It is a theory which describes the strong, electromagnetic and weak forces but does not currently provide a description of the force of gravity. In the standard model, the elementary particles can be divided into two groups: the fermions and the bosons. The fermions and bosons are delineated by their intrinsic angular momentum known as their spin. The fermions have half-integer spins while the bosons have integer spins. Particles composed of other particles may be a fermion or a boson depending on their total spin state. The quarks and leptons are both fermions while the mediators of the strong, weak and electromagnetic force are bosons. These fundamental forces are carried by the gluon (strong), the W and Z bosons (weak) and the photon (electromagnetic). In the standard model, there is also another fundamental boson which is not a mediator of a force, and that is the Higgs boson [4]. The Higgs has not been observed in experiments but it is theorized to be key in explaining the origins of masses and the differences in the masses of the mediator bosons. The fermions themselves are divided into three generations (Table 1.1), where ordinary matter consists of the stable first generation fermions. As the generation increases, so does the mass. The first generation particles are stable whereas the second and third generation particles will decay to first generation particles. As can be seen in the table, the leptons and quarks have integral and fractional charge, respectively. The colour quantum number is the defining feature of the strong force with the quarks having non-zero colour of red, green or blue. This lead to the theory of quark confinement which states that all naturally occurring particles are colourless, which means that the leptons have zero colour charge.

The neutrinos, ν_e, ν_μ, and ν_τ, have no charge and and were thought to be massless until recently. The neutrino was seen to change its flavour from as it propagates from the core of the sun to the Sudbury Neutrino Observatory, which can be explained by neutrino oscillations requiring a mass difference between the different

Table 1.1: The Elementary Particles & their categories

Generations	I	II	III	Charge
Leptons	ν_e	ν_μ	ν_τ	0
Leptons	e^-	μ^-	τ^-	-1
Quarks	d	s	b	-1/3
Quarks	u	c	t	2/3

$$\begin{pmatrix} d' \\ s' \\ b' \end{pmatrix} = \begin{pmatrix} V_{ud} & V_{us} & V_{ub} \\ V_{cd} & V_{cs} & V_{cb} \\ V_{td} & V_{ts} & V_{tb} \end{pmatrix} \begin{pmatrix} d \\ s \\ b \end{pmatrix}$$

Figure 1.1: The Cabibbo-Kobayashi-Maskawa matrix.

neutrino flavours [5]. The lack of charge allows the neutrinos to pass through most matter without interacting. This poses a challenge as the neutrino can carry away a significant amount of energy in a particle decay. In practice the vector sum of the neutrinos, represented by an imbalance in the total transverse momentum in the event, is known as the missing transverse energy ($\not{E}_T$). The transverse momentum is used due to physical restrictions on where detection equipment can be placed relative to the direction of the beam. The leptons and quarks both have anti-particle counterparts, which are the negative energy solution to the Dirac equation [6], the relativistic quantum mechanics equation for the energy. The anti-quarks play an important part in the formation of anti-baryons and mesons. As an example, the proton is a baryon formed from the combination of (uud) quarks while the J/ψ is a combination of ($c\bar{c}$).

The forces in the SM are mediated by an exchange of a particle, the bosons. In

$$\begin{pmatrix} |V_{ud}| & |V_{us}| & |V_{ub}| \\ |V_{cd}| & |V_{cs}| & |V_{cb}| \\ |V_{td}| & |V_{ts}| & |V_{tb}| \end{pmatrix} = \begin{pmatrix} 0.97377 \pm 0.00027 & 0.2257 \pm 0.0021 & 0.00431 \pm 0.00030 \\ 0.230 \pm 0.011 & 0.957 \pm 0.017 & 0.0416 \pm 0.0006 \\ 0.0074 \pm 0.0008 & 0.0406 \pm 0.0027 & > 0.78 \end{pmatrix}$$

Figure 1.2: Values taken from Volume 33, July 2006 of the Review of Particle Physics [16]

Quantum Electro Dynamics (QED), the mediator for the electromagnetic force is the photon, which couples to charged leptons. All force processes can be reduced to an elementary primitive vertex. A primitive vertex is simply the smallest interaction possible with the mediator, which forms a vertex that can be glued together with other primitive vertices to form more complex interactions. The electromagnetic primitive vertex is shown in Figure 1.3a, where l is a lepton and γ is the photon. In Quantum Chromodynamics (QCD), the mediator for the strong force is the gluon which couples to coloured particles, much as the photon couples to charged particles. In this case, since only quarks and gluons carry colour, the primitive vertex is shown in Figure 1.3b, where q is a quark and g is a gluon. In weak interactions, the mediators for the weak force are the charged W's and the neutral Z's, which participate in charged and neutral interactions respectively. The fundamental weak, charged, primitive vertex is shown in Figure 1.4a, where l is a lepton, ν_l is a lepton neutrino and W is our charged mediator. Similarly, the neutral primitive vertex uses the Z as a mediator and is shown in Figure 1.4b, where the particles ν_l can also be leptons as the Z couples to both. The weak force also interacts with quarks but does not conserve the flavour of the quarks in Table 1.1, but in fact, couples the known quarks in what is know as the Cabibbo-Kobayashi-Maskawa matrix [7] shown in Figure 1.1. This is a 3×3 matrix which says that the weak force does not simply couple u-d (up-down), c-s (charm-strange), and t-b (top-bottom quarks). Instead, it couples u-d', c-s', and t-b', where the d', s', and b' quarks are linear combinations of the actual d, s, and b quarks, describing the mixing of weak and flavour states of particles. It has been found experimentally that the CKM matrix is not the identity matrix (Figure 1.2), which accounted for the cross-generation transitions such as a strange quark going to an up quark in reaction $\Lambda \rightarrow p^+ + \pi^-$. The values of the matrix can have imaginary numbers which is an indication of the amount of CP violation. CP symmetry is the symmetry of charge conjugation, which converts a particle into its anti-particle, and parity, which mirrors the physical world reversing left and right handedness. A violation of CP is incorporated in the SM through the CKM matrix by the introduction of a complex phase. It is thought to be the reason

for the imbalance of matter and antimatter in the universe.

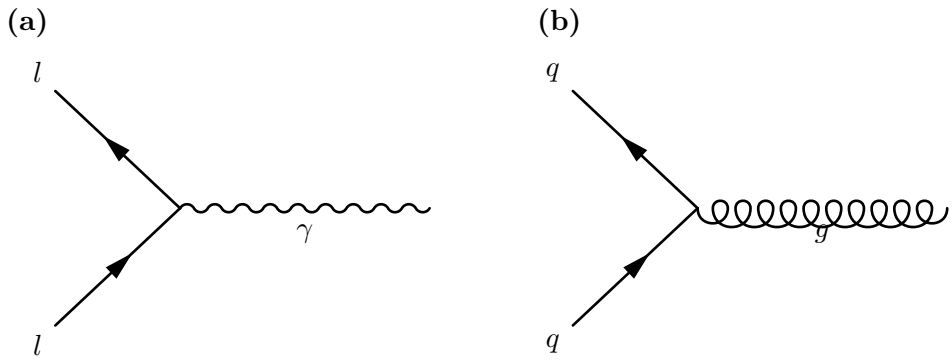

Figure 1.3: Feynman diagrams for the primitive vertex of: (a) the electromagnetic force with propagator γ, and (b) the strong nuclear force with propagator g.

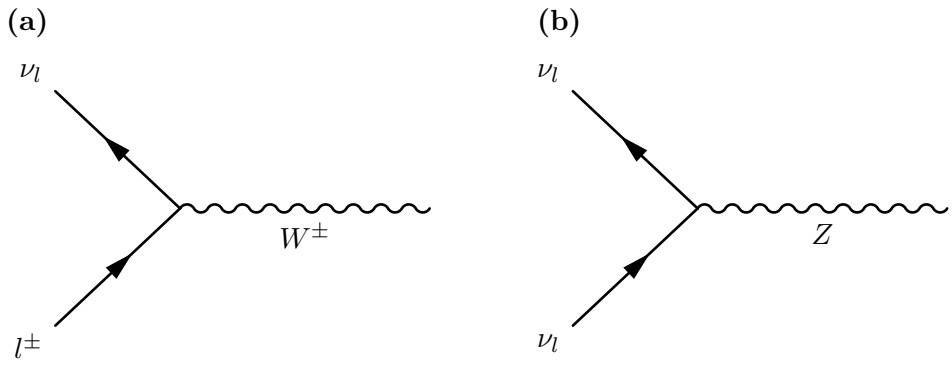

Figure 1.4: Feynman diagrams for the lepton primitive vertex of the weak force with propagator: (a) W boson, and (b) Z boson.

So far, the Standard Model has successfully predicted many quantities and has withstood the test of time for its theoretical prowess. There is, however, still one predicted particle left unobserved and that is the Higgs boson. The SM Higgs "field" is a scalar field which has a non-zero expectation value within the vacuum. This vacuum expectation value is thought to be the mechanism through which all elementary particles acquire mass and is important in understanding the breaking of the electroweak gauge symmetry. The force mediators are expected, in the SM, to be symmetric. This symmetry is required for the unification of the weak and electromagnetic forces into an electroweak force, and does not allow for the mediators

to have a non-zero mass. Unfortunately, unlike the photon, the W and Z bosons have masses of 80 GeV and 91 GeV respectively which breaks the symmetry in what is known as electroweak symmetry breaking. Although the Higgs itself has not been found, indirect bounds for the mass of the Higgs boson may be found from fits to electroweak observables such as the t-quark and the W mass. The t-quark was the last quark that was predicted by the SM, but had not been experimentally verified. The discovery of the t-quark in 1995 by the CDF and D0 collaborations brought the first available data for the electroweak fitting and found the mass for the top quark to be $m_t = 178 \pm 8_{stat} \pm 10_{syst}\ GeV/c^2$ for CDF [8] and $m_t = 199 \pm 20_{stat} \pm 22_{syst}\ GeV/c^2$ for D0 [9], where the first uncertainty is from the sample size statistics and the second uncertainty is from the systematic uncertainties. The fit for the bounds on the Higgs mass is sensitive to $log(m_{H^0})$ where the best fit for $m_{H^0} = 91^{+45}_{-32}\ GeV/c^2$, with the mass value $< 186\ GeV^2$ with a 95% confidence level [16]. The top quark, with the most recent mass measurement of $m_t = 171.4 \pm 1.2_{stat} \pm 1.8_{syst}\ GeV/c^2$ [10] from up to 1 fb^{-1} of data, also tends to play a special role in the dynamics of symmetry breaking in models beyond the SM. This, along with confirming another cornerstone of the SM, is why the discovery of the top quark by the DØand CDF collaborations has been so important.

1.2 The Single Top Quark

In hadron colliders like the Tevatron, the top quark is produced predominantly in pairs through the QCD processes of $q\bar{q} \rightarrow t\bar{t}$ and $gg \rightarrow t\bar{t}$. At the Tevatron energies of 1.96 TeV, and with a mass of $m_t = 175\ GeV/c^2$, the pair production cross section is expected to be $6.7 \pm^{0.71}_{0.88}\ pb$ combined for the s-channel and t-channel [11]. Pair production of top quarks allow act as an excellent probe into the QCD properties of the top quark, but production of a single top quark will allow for a study of its electroweak interactions. The single top has three predominant modes of production with three different cross sections at the Tevatron for a mass of m_t = 175 GeV: the t-channel Figure 1.5 (2.4 pb), the s-channel 1.6a (0.86 pb) and the tW^- mode of production Figure 1.6b (0.088 pb) [17]. This is far less than the $t\bar{t}$

cross-sections, and with both involving the creation of t-quarks, the $t\bar{t}$ provide a significant background for single top identification.

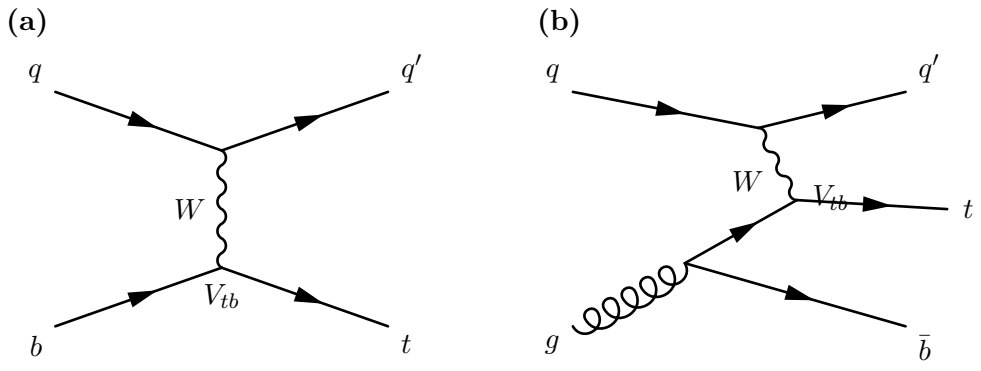

Figure 1.5: Feynman diagrams for the t-channel: (a) leading order diagram with a t, and a q' quark produced and (b) an NLO diagram with a t, a q' and a $\bar{b}$ quark produced.

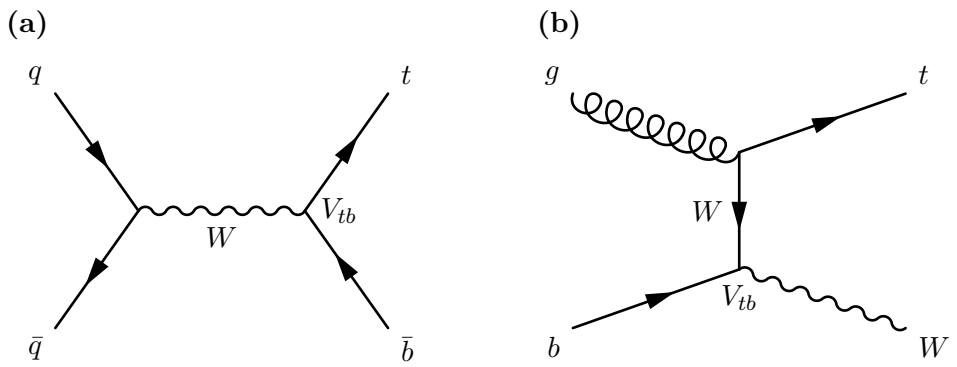

Figure 1.6: Leading order Feynman diagrams for the (a) s-channel and (b) tW^- process for the production of a single top quark.

As can be seen in Figure 1.5 and 1.6, the production of the single top depends strongly on the CKM matrix element V_{tb}. The value of $|V_{tb}|^2$ from the CKM matrix can be extracted directly from a measurement of the cross section which is also one part of the complex number $V_{tb} \times V_{tb}^*/V_{cb} \times V_{cb}^*$. The decays of the B^0 meson also depend on the CKM matrix element V_{tb} [12], and so the single top measurements can provide another measurement of this number.

Due to the predicted cross sections for single top at the Tevatron, the tW^- mode

of production is far less likely to be detected when compared with the relatively abundant t and s-channel production. The discovery of the single top is further hampered by the abundant background events that share a similar signature to the signal events; pair production of top quarks is one such background. To understand the background events that hamper the discovery of the single top, the signature of the single top must be understood. In the t-channel (Figure 1.5a), a q'-quark and a t-quark is produced as the leading order production, with a similar process with the b-quark provided by a gluon (Figure 1.5b). In the s-channel (Figure 1.6a), a t-quark and a $\bar{b}$ quark are produced. In any case, a quark that is produced, that is not the t-quark, which will tend to undergo hadronization; the process in which a quark, through the asymptotic freedom of the strong force, fragments into a quark anti-quark pair. These quark pairs can further decay in a repeated process until what remains is a cluster of colour-neutral mesons and baryons known as a *jet*. The momentum of the original quark, carries the jet into the detector and it is seen in the calorimeters as a cone shaped deposit of energy. The t-quark, however, does not undergo hadronization due to its short decay lifetime of $< 10^{-24}$ s [13]. Since the single top is a free quark that decays instead of undergoing hadronization, the spin states of its decay products are determined by the spin state of the t-quark [14] which can then be used to test the predictions of the spin polarization of quarks. As well, the s and t-channels are sensitive to different new physics decays such as the flavour changing neutral current (FCNC) decays of the top quark. These FCNC decays, such as $t \to q\gamma$, are suppressed in the SM and are not observable in the current or near future particle colliders. The observation of these decays would be an indication of new physics.

The dominant decay ($\approx 100\%$) of the t-quark is given by $t \to Wb$, which is the primary weak vertex for the W boson, and the b and t quarks. The other decays involve a change in the quark flavour by converting the t-quark into an s-quark ($t \to Ws$) or a d-quark ($t \to Wd$) which have not been observed in experiments. The b-quark produced in this decay will undergo hadronization into a jet while the W boson may decay into a lepton (l) and a lepton neutrino (ν_l), preferably an

electron or a muon with their associated neutrinos ($e + \nu_e$ and $\mu + \nu_\mu$). The decay of the b-quark will produce a jet from a vertex that is displaced from the main interaction vertex. The W boson may also decay into a q-$\bar{q}$ pair, but this will not provide a good search signature since the two quarks will hadronize into jets. Due to the decay signature of the single top events, the signal is obscured by a number of backgrounds, one of which is the $t\bar{t}$ production.

Chapter 2

The DØ Detector

2.1 An Overview of the Detector

The DØ Detector collected data from 1992-1996 known as Run I, of proton anti-proton collisions at a center of mass energy of $\sqrt{s} = 1.8$ TeV [18], leading to the discovery of the top quark among others. The Tevatron was then upgraded and began running again in 2001 where this later period is known as Run II. During Run I, the peak luminosity provided by the Tevatron was typically 1.6×10^{31} cm^{-2}s^{-1} [19]. This was produced as six bunches of protons and anti-protons with a 3.5 us gap between bunch crossings. During this first run, the DØ detector recorded 140 pb^{-1} of integrated luminosity [19]. After the Tevatron was upgraded with a new Main Injector, the Tevatron operated with 36 bunches of protons and anti-protons with only a 396 ns gap between bunch crossings, and with a center of mass energy of $\sqrt{s} = 1.96$ TeV [18].

The DØ Detector was upgraded in order to process the larger amount of data from the upgraded Tevatron. The following is an introduction and broad overview of the detector which will be explored in detail in the later sections of this chapter. The tracking, calorimetry and muon systems will be discussed which will be followed by a discussion of the triggering system. The upgraded DØ detector consists of three detector subsystems surrounding the beam pipe in which the proton anti-proton collisions occur, where the scale of the components can be seen in figure 2.1. The central tracking detectors are closest radially to the beam pipe, consisting of the Silicon Microstrip Tracker (SMT), the Central Fibre Tracker (CFT), a 2 T solenoidal

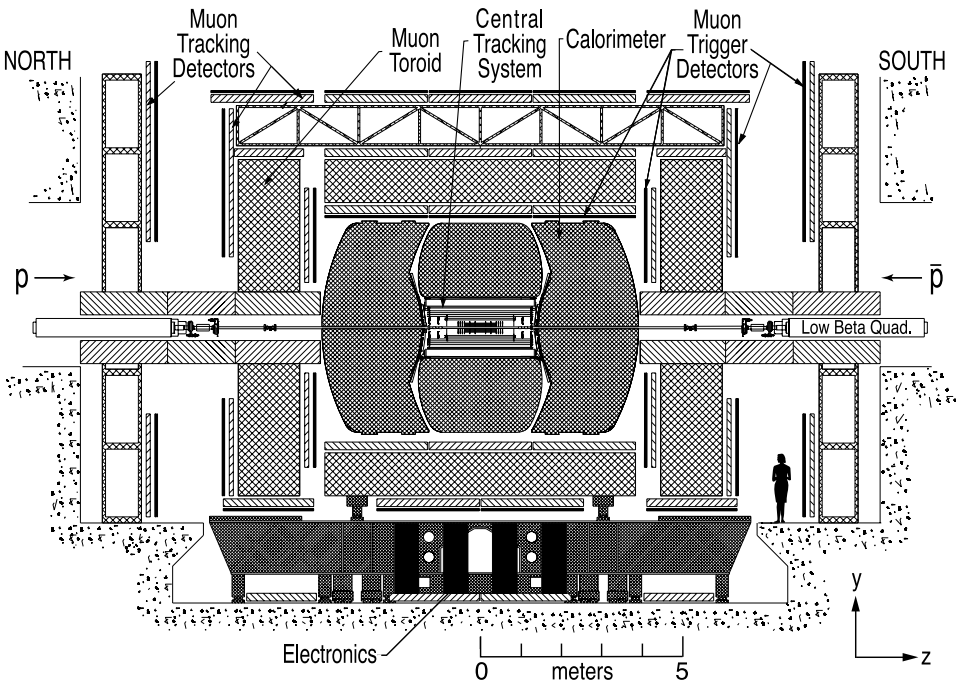

Figure 2.1: The beam pipe, the tracking system, the calorimeters and the muon system. [20]

magnet and the preshower detectors. Moving out from the preshower detectors are the uranium/liquid-argon calorimeters which consists of a Central Calorimeter (CC), an End Calorimeter North (ECN), and an End Calorimeter South (ECS). The tracking and calorimetry systems are then surrounded by the muon detection system, which consists of toroidal magnets, the Central Muon Detector and the Forward Muon System.

The addition of new detector components for Run II, along with the increased luminosity and the reduction in the bunch spacing required an improvement of the data acquisition system. To this end, the readout electronics have been improved and the trigger system has been enhanced. The trigger system is a decision making system which decides whether to keep or discard a detected collision event. It is a hardware and software system which emphasizes speed in order to handle the significant amount of data coming from the detector. Such a system is required since the 7 Mhz of collision data would require writing out at a rate and storage capacity that are far beyond the capabilities of the system. The trigger system is still

expected to reduce the data rate to 50 hz before it it written to tape. The trigger consists of three trigger levels; a hardware level (Level 1 or L1), a combination of hardware and software level (Level 2 or L2) and software level (Level 3 or L3) which is the slowest of the three. Acceptance of an event within the L3 trigger requires acceptance from the previous triggers. The three distinct levels allow for more complexity in the algorithms used to determine which events should be stored for further analysis and which are unimportant.

In the following subsections, a right handed coordinate system is used: the z-axis is along the proton direction, the y-axis is upwards, the angle ϕ is the azimuthal angle, the angle θ is the polar angle which is represented by the pseudorapidity $\eta = -\ln\tan\theta/2$, and the r coordinate is the perpendicular distance from the z-axis.

2.2 The Tracking System

The Central Fibre Tracker (CFT) and Silicon Microstrip Tracker (SMT) are the tracking detectors which are used to locate the primary vertex of the collision event, measure the tracks of particles and are used to match these tracks to objects in the calorimeter and muon systems. This is accomplished by linking detector hits together and projecting them back to the interaction point. The tracking detectors can locate the primary vertex to a resolution of 35 μm [18]. They also provide an accurate measurement of the lepton p_T, the jet E_T, the $\not{E}_T$, and can tag b-quark jets with an impact parameter resolution of 15 μm [18]. The solenoidal magnet is used to provide a way to measure the momentum of particles, optimize the momentum resolution, $\delta \mathrm{P}_T/\mathrm{P}_T$ and tracking pattern recognition. This is accomplished by the creation of a nearly uniform (the near uniformity is shown in figure 2.2) 2 T magnetic field within the tracking chamber. The trajectories of charged particles will bend in the magnetic field, and it is this curved track that provides a measurement of the momentum. The large strength of the magnetic field will cause a larger bend in the track which enables for a high momentum resolution. The magnetic field also serves to seperate particles where the seperation distance will increase as

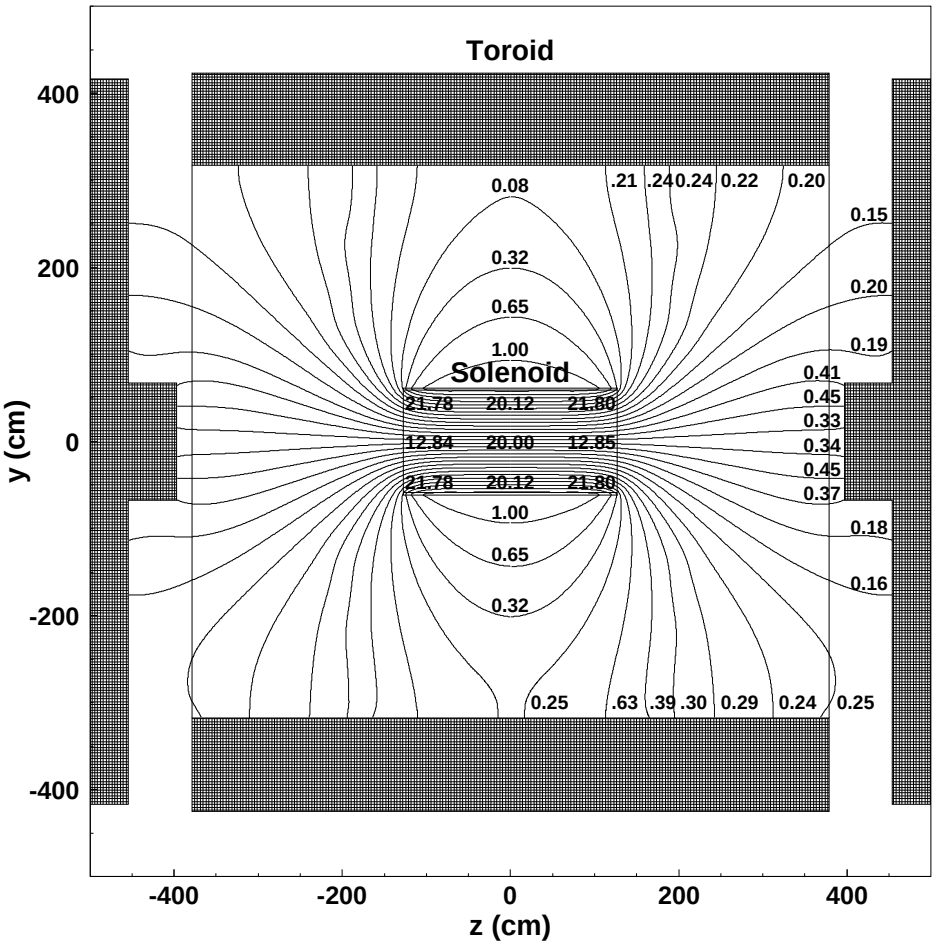

Figure 2.2: y-z view of the magnetic fields for the toroidal and solenoidal magnets in units of kG. The central toroid is approximately 1.8 T while the end toroids are about 1.9 T. [20]

the magnetic field increases. The fourth components of the tracking system are the preshower detectors. The preshower detectors can function as calorimeters and also provide accurate position measurements. This enhances matching between tracks and calorimeter showers, which aid in electron identification and background rejection during triggering and offline reconstruction. These systems and their physical relationship to the calorimeters are shown in figure 2.3.

The SMT, located radially near the beampipe, provides for high resolution vertex and track reconstruction, for over nearly the full η range, $|\eta| < 3$, where η is the pseudorapidity. The detection of these charged particle tracks is accomplished by

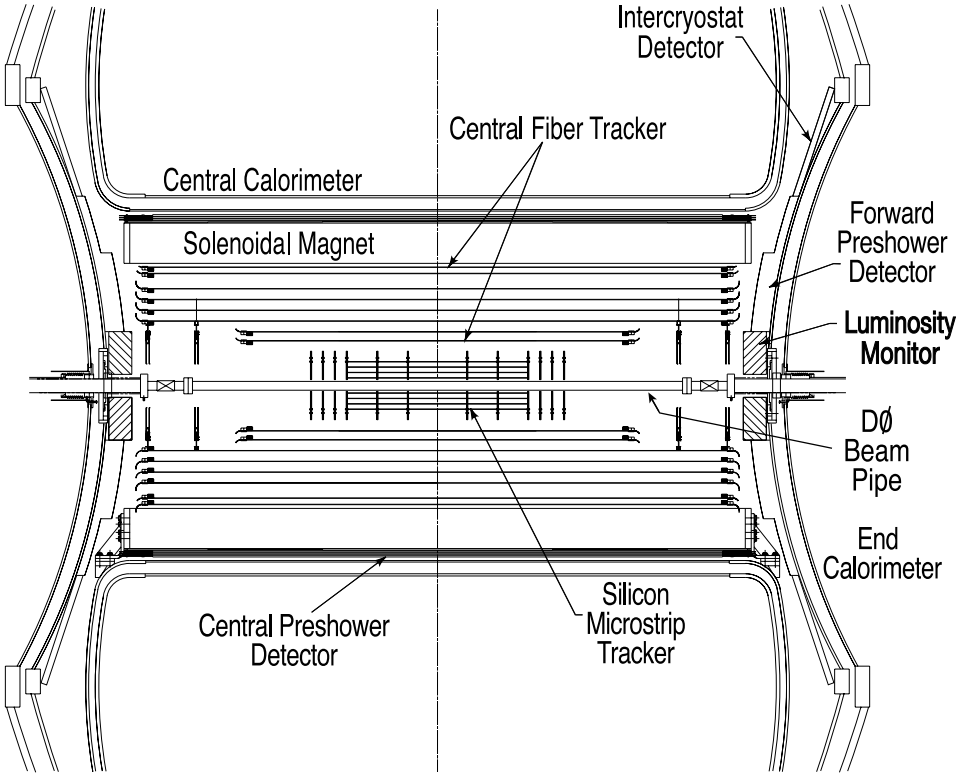

Figure 2.3: The tracking systems which include the Central Fibre Tracker, the Silicon Microstrip Tracker, the Preshower Detectors and the Solenoidal Magnet. [20]

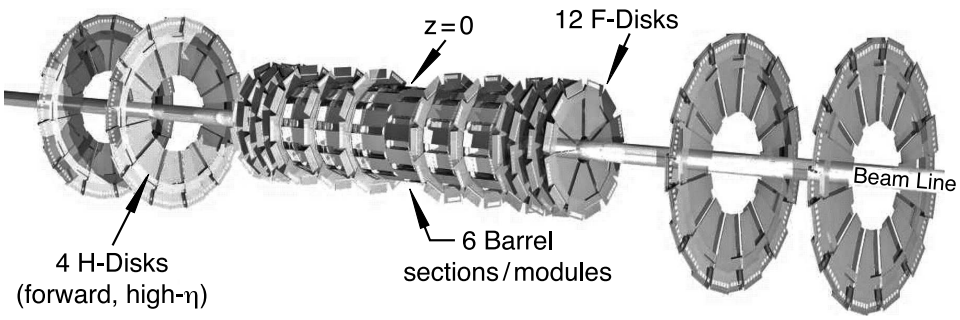

Figure 2.4: The barrel and disk detectors used for the Silicon Microstrip Tracker. [20]

creating a depletion zone, a region without charge carriers, within the silicon. When a charged particle enters the silicon, it ionizes the silicon, which produces a signal to a connected electrode. This will provide one or two coordinates for single or double sided silicon wafers. To maximize the accuracy of this detection, the detector was designed to minimize the number of tracks that hit the detector surfaces at shallow angles for all of η; this required a combination of barrel and disk detectors. In the central region covering $|\eta| < 2$, six 12 cm long barrels with 4 detector layers each, are used. These measure the $r - \phi$ coordinates. These are further layered by 12 disk detectors, which surround and cap each barrel called F-disks which measure the $r - z$ as well as $r - \phi$. Farther along the beampipe from the center, sit two larger disks on either side of the barrel detectors and F-disks (Figure 2.4). These larger disks are called H-disks and cover the remaining region of $2 < |\eta| < 3$ [18]. This minimizes the number of tracks which will hit the surface of the detector at a shallow angle; barrel detectors for tracks of low η and disk assemblies for tracks of high η. The SMT sends the signals it recieves to the Level 2 and Level 3 triggers, so that the information can be used to trigger on displaced vertices from b-quark decay.

While it is required for the SMT to be high resolution, given its proximity to the beampipe, the CFT is situated radially outward from the SMT and thus farther from the beampipe. This extra distance provides for the detector to be constructed of scintillating fibres, which have a lower accuracy than the silicon microstrips of

the SMT. When a passing charged particle encounters one of these fibres, they emit light with a frequency of 340 nm, which is absorbed by a wave-shifter and re-emitted at 530 nm. This wave-shifted wavelength of light is well transmitted in the polystyrene core of the fibres. This light then travels through clear fibre waveguides and is collected by Visible Light Photon Counters (VLPC). These are impurity-band silicon avalanche photodetectors that sit in a cryostat of liquid helium, and operate with a maximum efficiency at a temperature of 9 K [18]. The VLPCs can detect single photons and work well in high noise environments, sending the electrical signals to the preamplifiers that sit on analogue front end boards (AFEs). Since the particle tracks will diverge due to their directions of travel and the magnetic field imposed on them, the scintillating fibres do not need to be as fine grained as the silicon microstrips. The CFT consists of eight concentric support cylinders which hold these fibres. The fibres themselves are 835 μm in diameter and 1.66 or 2.52 m in length, which are formed into layers. Doublet layers are formed by aligning the fibre centers of one layer with the spaces between the fibres on a second layer. Each of the eight support cylinders houses a doublet layer of fibres aligned along the beam axis (axial layers) and at a stereo angle (stereo layers) of u (+3°) or v (-3°). From the VLPC converted electrical signals sent to the AFEs, the CFT is able to provide a fast and continuous readout of discriminator signals to the Level 1 trigger system. If Level 1 accepts the event, it sends track information to Level 2 for triggering. Level 3 recieves a slower readout of the digitized analog signals, in addition to Level 1 and Level 2 information.

Around the tracking detectors are the preshower detectors; the Central PreShower detector (CPS) covering the central region of $|\eta| < 1.3$ and the two Forward PreShower detectors (FPS) covering the end regions of $1.5 < |\eta| < 2.5$, on the faces of the end calorimeters. The preshower detectors provide fast energy and position measurements, before the particles undergo a shower, which can be used at L1 for triggering. They work much like the CFT in that they use scintillating fibres and VLPCs to provide a readout. While the CPS works much like the CFT, the FPS is a little different. In the FPS, charged particles pass through 2 layers: the Minimum Ionizing

Particle (MIP) layer and shower layers past the absorber. Charged particles will pass through the MIP layer and register minimum ionizing signals which provide a measure of the location of the track. Electrons will shower (a shower will be defined in the calorimeter section) in the absorber which will be detected in the shower layer and can be matched spatially with a MIP layer signal. Photons may not interact with the MIP layer but will tend to shower in the shower layer, and heavier charged particles are less likely to shower at all, prodicing another MIP signal in the shower layer.

2.3 The Calorimeters

The calorimeters are used to measure the energy of the electrons, photons and jets in the absence of a magnetic field, as well as measure the transverse energy balance in events. They also assist in object identification of the electrons, photons, jets and muons, as well as providing an estimate of the energy missing from the event from low-interacting particles such as neutrinos. The calorimeters remain unchanged from Run I, even with the addition of the 2 T solenoidal magnet. The calorimeters are uranium - liquid argon ionization detectors, which detect particle showers. A particle shower occurs when a particle interacts with a material through scattering, creating a photon which can decay through pair production. The resultant secondary particles may further interact with material creating a cascading shower of particles. With further cascades, the energy will be low enough to be absorbed through ionization in the material. Muons, being more massive than electrons, will tend not to shower in such a way as their mass lowers the probability of a cascading energy loss through scattering.

The calorimeter is split into three separate cryostats, which weigh 300 metric tons and contains 15,000 litres of liquid argon: a Central Calorimeter (CC, covering $|\eta| < 1$), and two End Calorimeters (EC, covering $1 < |\eta| < 4$) [18]. The use of three seperate cryostats provides for easy access to the CC, and ECs when pulled apart. Each cryostat is further segmented into three regions: an electromag-

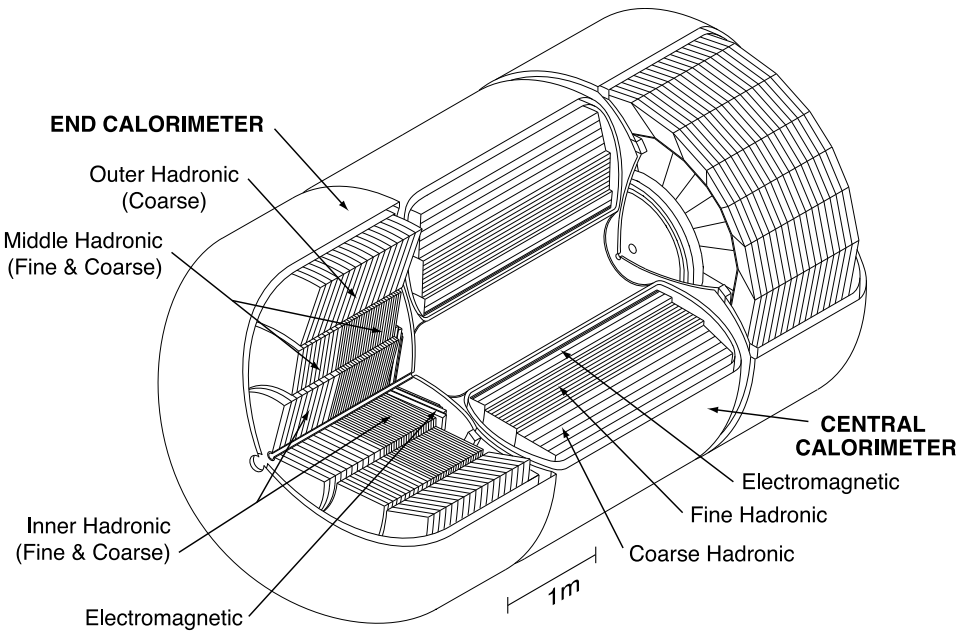

Figure 2.5: The segmented regions of the calorimeter: the outer, middle and inner hadronic regions, and the electromagnetic regions. [20]

netic (EM), followed by a fine hadronic (FH) region, and a course hadronic (CH) region further out, which are shown in figure 2.5. Such a calorimeter is known as a compensating calorimeter which uses methods such as varying the thicknesses of absorber plates in order to achieve an electron:hadron ratio of 1:1. This ratio is the difference in response signals of the calorimeter from EM and hadronic particles of the same incident energy and a ratio of 1 is required for a linear energy response during hadronic showers. A calorimeter optimized in such a way is able to achieve an energy resolution which improves with increasing incident energy and was the goal of the calorimeters. Each region uses different absorbers: 3 mm (CC) or 4 mm (EC) depleted uranium plates in the EM section, 6 mm uranium-niobium plates in the fine hadronic section, and 46.5 mm copper (CC) or stainless steel (EC) plates in the coarse hadronic section. The use of three separate cryostats for the calorimeter, leads to gaps in the range of the pseudorapidity covered ($0.8 < |\eta| < 1.4$). Within these gaps sits a scintillating layer known as the Inter-Cryostat Detector (ICD), which covers a region of $1.1 < |\eta| < 1.4$. The ICD provides sampling in an otherwise unsampled area which would have degraded the energy resolution. Particles

traversing the high density uranium can either cause an EM shower or in the case of hadrons, cause a hadronic shower through inelastic scattering. The shower of charged particles from the uranium then ionizes the liquid argon and the charge drifts to signal boards 2.3 mm from the absorber plates with a charge collection time is 450 ns [18]. The absorber plates and signal boards all sit within a liquid argon cryostat and this mechanism makes up the calorimeters.

The readout cells for the calorimeter form pseudo-projective towers, named for the fact that the center of each cell lies on a ray that projects from the center of the interaction region (Figure 2.6). Each readout cell has a transverse size comparable to that of the showers: 1-2 cm for EM showers, and farther out, 10 cm for hadronic showers which increase in size for larger values of η to avoid having very small cells. The readout cells form a tower of $\Delta\eta \times \Delta\phi$, where $\Delta\eta = 0.2$ and $\Delta\phi = 0.2$. The energy within these 0.2×0.2 towers are used in the L1 and L2 calorimeter triggers. The signals from the detector are transferred to charge preamplifiers, which send the signal to be digitized in signal shapers and then sent to storage circuits. The signal is held for the Level 1 trigger decision for 4 μs in analogue storage devices (switched capacitor arrays), which are located below the cryostats. The signal is held further for the Level 2 trigger decision for an additional average time of 2 ms, with a maximum time of 25 ms. Precision signals from the storage is then transmitted to the data acquisition system for an L3 decision.

2.4 The Muon System

Muons are much like electrons in that they have the same charge but are around 200 times more massive than an electron. This means that they lose for less energy than an electron when passing through matter, and so they pass through the calorimeters and the pre-shower detectors freely. It is for this reason that the muon detection system is the farthest out radially from the collision event and it is designed with the intention of detecting muons which travel through the rest of the detector. To detect the incoming muons, the muon system is split into a central muon system,

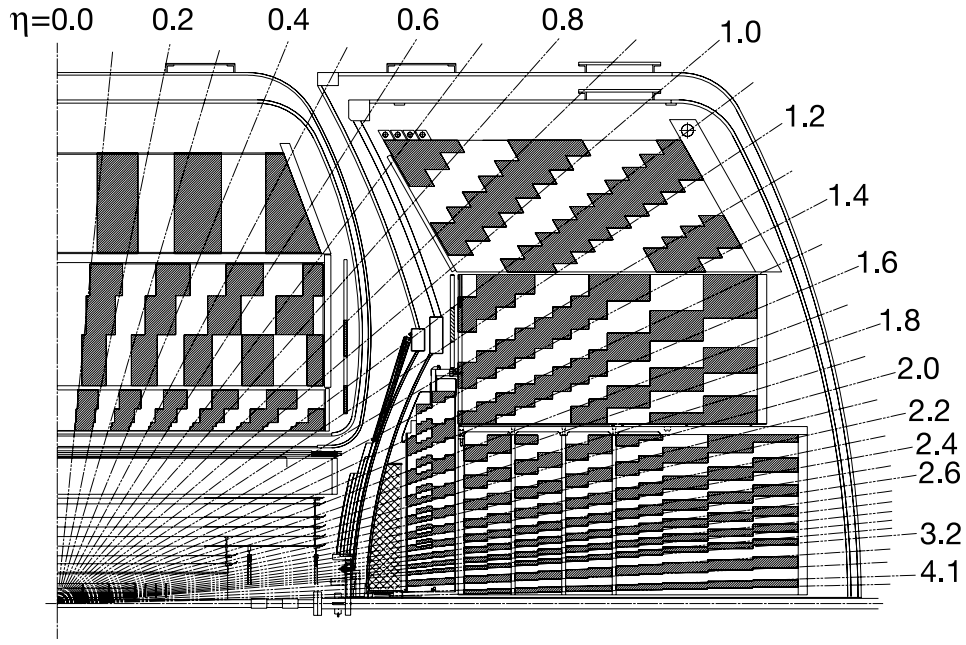

Figure 2.6: The pseudo-projective towers which form the cells that together constitute a signal readout. [20]

covering $|\eta| \leq 1.0$, and a forward muon system, which covers $1.0 \leq |\eta| \leq 2.0$ [18]. The central and forward muon systems use drift tubes, which are cylinders of gas which can be ionized by a muon surrounding a central high voltage wire used to generate and detect the signal.

The central muon system uses Proportional Drift Tube (PDT) chambers, a toroidal magnet, the cosmic cap, and scintillation counters for triggering on muon events. The toroidal magnet allows for better triggering on the muons and a measurement of the p_T which is independent of the calorimeter system. The PDT system itself registers hits which record the electron drift time, the difference Δt in the arrival time of the signal pulse and the readout of the signal which has a maximum of 450 ns, and the charge deposition. The cosmic cap provides a fast timing signal which can be used to associate a muon hit in the PDT with the appropriate bunch crossing. Since the cosmic cap covers the top and bottom of the detector, it can also detect hits which pass through the top and bottom to reject them as hits from the cosmic ray background. The PDT system is also supported by sets of scintillation

counters on the top, upper sides, lower sides, and bottom of the central muon drift tubes. These provide for an association between a muon in the PDT with the bunch crossing from whence it came, which provides additional background rejection.

The forward muon system uses three layers of Mini Drift Tubes (MDT), end toroidal magnets, three layers of scintillation counters and shielding around the beam pipe for the muon system. The MDTs are similar to the PDTs, but have a shorter electron drift time below 132 ns [18]. The toroidal magnets work in the same way as with the central muon system, and allow for the measurement of the muon momentum. The system itself is not as good as the central tracker but provides for low resolution tracking and identification of muons.

2.5 The Trigger

Due to the high interaction rates of particles at the Tevatron, from high luminosities and energies of the incoming particles, a three tiered trigger system was implemented. The three levels of the trigger system were chosen due to the speed of the readouts of the different detector components discussed. The goal of the trigger system was to filter the incoming data into a more manageable size for data storage. At Level 1 (L1), the detector subsystems have only a short period of time to make available the information necessary to determine an accept for the event (35 μs or less). The rate of data accepted at L1 provides the Level 2 (L2) trigger system a greater amount of time to make a decision. This additional time is used by the detector subsystems to either send a more complete readout of the data to L2 or to hold the data in storage for Level 3 (L3), at which time the trigger system will have access to the full readout of the detector subsystems.

The three distinct levels form a trigger system which accepts events at a lower rate at every level, but with a greater allowed complexity for the determination of an accepted event at the higher trigger levels. The rate of trigger accepts at L1, L2 and L3 are about 2 kHz, 1 kHz, and 50 Hz respectively [18]. The trigger framework (TFW) interacts with L1 and L2 which determines the events that are passed to

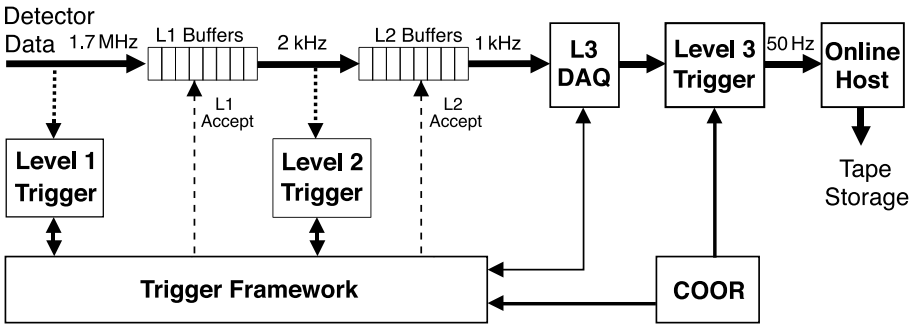

Figure 2.7: The Trigger Framework and its relation to Level 1, Level 2, Level 3, and the data acquisition system. [20]

L3, shown schematically in figure 2.7. The first level (L1) is a hardware trigger that filters over simple variables such as the existence of a charged lepton. The second level (L2) is a combination of hardware and software which obtains a greater readout from the detector subsystems and can use this readout along with the information from L1. This allows for trigger decisions to be made based on individual objects such as electrons, muons, and jets, as well as correlations between the objects. The third level (L3) is sent candidates that have passed the L1 and L2 triggers, along with the full readout of each detector subsystem. At L3, physics objects and relations between the objects are generated by software algorithms called filter tools. The event is crudely reconstructed by these filter tools, and accepted events at this level are written to tape for offline reconstruction.

2.5.1 Level 1 trigger

The L1 trigger is a hardware trigger which examines every event, where an event is a collision or bunch crossing within the detector, and determines an interesting event from 4 subsystems: L1CAL, L1CTT, L1MUO and L1FPD. Within TFW for L1, 128 specific triggers can be programmed using up to 256 "AND-OR" terms which determines whether a given bunch crossing meets the conditions required to pass the trigger. Elements of the L1 trigger are allowed to be AND'd and OR'd together to form pseudo-terms. These will increase the efficiency of the triggers which may reduce backgrounds or the rate from low-p_T triggers. The L1CAL subsystem consists

of the EM and hadronic energies which are formed into trigger towers from sums, in depth, and in transverse coordinates ($\Delta\eta \times \Delta\phi = 0.2 \times 0.2$) which were described earlier for the calorimeter. The EM transverse energies and the total transverse energies (EM and hadronic) are used as variables for the trigger, which are converted from the tower energies into E_T on input which also use ICD towers in the trigger calculations. The upgraded L1CAL subsystem had a set of trigger thresholds: 4 for the EM tower energy, and 4 for the total energy (EM + hadronic). Requirements, such as requiring 2 towers over a certain energy, are used in the trigger calculations. Future implentations at L1 will use a clustering algorithm to determine the proximity of one tower with an energy deposit to another. The L1CTT subsystem uses the discriminator data provided by the CFT, the CPS and the FPS detectors to perform simple reconstruction of the trajectories of charged particles, which also triggers on the STT subsystem from the STT/SMT. The discriminator data provided are logic bits that are generated from wire signals from the subdetectors. L1CTT triggers on the tracks reconstructed in firmware which can be matched with EM cluster energy from the CPS detectors, while the FPS detector triggers on EM clusters on the FPS. The L1MUO subsystem uses the muon wire chambers, the muon scintillation counters and the tracks provided by L1CTT to look for muons within the event. Finally, the L1FPD subsystem can trigger on events using a combination of the nine FPD spectrometers, but it is currently not used in online triggers. As an example, the trigger MUW_W_L2M3_TRK10 has an L1 condition requiring a wide region, tight scintillator trigger, with a loose wire requirement for the muon.

2.5.2 Level 2 trigger

The L2 trigger is a combination hardware and software trigger which analyzes the inputs from events that have passed L1. The events are selected by a processor known as L2Global, which uses the 128 specific triggers applied at L1. As a starting point, inputs from the calorimeter, CFT, CPS, FPS, SMT and muon subsystems are put through preprocessors which reconstruct the objects. These are then sent to the L2Global processor to decide whether an event has passed the trigger. There are L2

preprocessors for each of the detector subsystems along with the L2Global processor: L2Cal, L2Muon, L2PS, L2STT, and L2CTT. The L2Cal preprocessor identifies jets, electrons, photons and is planned to also calculate the transverse energy (E_T) in the calorimeter. The L2Muon preprocessor refines the muon candidates from L1 and contains the track p_T, η coordinates, ϕ coordinates, and quality and timing information. The L2PS preprocessor provides information on early shower development, and allows for a comparison with the calorimeter clusters or tracks that are found. The FPS detector also functions as a source of forward tracking, which is the only available source before L3. The L2STT preprocessor reconstructs charged particle tracks found in the CFT at L1 by using data from the SMT, which allows it to tag the decays of long-lived particles. The hits required in the SMT help reject the false track patterns found in the CFT and provide a more precise measure of the tracks and impact parameter of the tracks. Finally, the L2CTT preprocessor takes the input from L2STT as well as L1CTT and provides a p_T and impact parameter sorted list of tracks to the L2Global processor for triggering.

The L2Global processor examines correlations across all of the listed detector subsystems from the preprocessors listed earlier. It does this by creating global physics objects, from these subsystem preprocessor objects, on which trigger decisions can be made. The trigger conditions are specified by a configuration file to which changes can be made for inclusion in the next run, of which a run is simply a period of time with stable beam and no change in the trigger conditions. This file can be downloaded to L2Global at the start of every run, and processes each event based on which trigger bits fired at L1. These trigger bits are associated, by the trigger list, to a script at L2 which contains the trigger condition that specifies whether an L2 trigger fired for that particular L1 bit. If any of the L2 scripts accepts an event, the event is accepted by L2 and is sent to L3. An with the example for L1, MUW_W_L2M3_TRK10, at L2 we require 1 medium muon with a $p_T > 3$ GeV. If these conditions are satisfied, the event passes L2 and is sent to L3 for additional rejection of events.

2.5.3 Level 3 trigger

The data from L2 is sent to the L3 framework which runs the trigger software on a distributed set of farm nodes. The farm nodes are controlled by ScriptRunner, which interfaces the L3 framework to the physics object tools. Each of these physics object tools has a reference set and a set of filter scripts: L3 jets and electrons, L3 muons, L3 missing transverse energy and L3 tracking. The reference sets define the physics objects and are input into the filter tools through the trigger list. These filter tools generate the physics objects and the relationships between them such as reconstructing leptons, vertices, $\not\!\!E_T$, and more. Through the trigger list and through these filters, conditions can be applied to the objects for the event to be accepted. The conditions, and order of the objects to be examined, are specified through the trigger list which will apply the L3 trigger for each L2 trigger bit that has been set; an event passes L3 if it passes all the filters for the given L2 trigger.

The L3 jets and electrons tool has the full calorimeter and primary vertex position readouts for its reconstruction algorithms. It applies a simple jet cone of $\sqrt{(\Delta\eta)^2 + (\Delta\phi)^2} = 0.25$, with a requirement on the transverse energy, an electromagnetic fraction > 0.9 and the transverse shower shape. The L3 muons use wire and scintillator hits to reconstruct the muon tracks, and matches the tracks to those in the central tracker. At this point, the cosmic ray top and bottom caps are used to recognize muon hits that have a timing which indicates that it is not from the collision event. The L3 $\not\!\!E_T$ tool calculates the $\not\!\!E_T$ by summing the calorimeter energy geometrically with sums of rings in pseudorapidity. It provides the ability to trigger on $\not\!\!E_T$, the ϕ angle of $\not\!\!E_T$, the total scalar E_T and the $\not\!\!E_T$ resolution in the event (called the $\not\!\!E_T$ significance). Lastly, the L3 tracking tool uses clustering algorithms on the hits in the CFT to form track candidates which exceed a minimum trigger p_T, and a modified method similar to the CFT is used for the tracks in the SMT. This tool provides a primary vertex for triggering, and together with the track information, it provides the overall L3 trigger system with the ability to have an increased efficiency for low E_T triggers. Continuing the example trigger of

MUW_W_L2M3_TRK10, at L3, we require a track with $p_T > 10$ GeV.

Chapter 3

Caf Trigger

3.1 Purpose

Physics analyses use data that is accepted by the DØ trigger System, with certain prescribed triggers for their area of analysis. The triggers used to obtain the final data contributes to the overall error in the final calculations from the data. The triggers are used to define and determine which events contain the relevant physics without losing events to incorrect identification of the relevant physics. The triggers will be biasing the accepted events so it is important to understand how the events are biased. The efficiency of a given trigger can be calculated as a function of various parameters and used to determine the probability of that trigger firing for a given event.

The *caf_trigger* package is based on the *top_trigger* [21] package used by the top quark analysis group at DØ, with the intention of providing a flexible and extendable trigger efficiency tool for other physics groups. Towards this end, it was designed from the ground up for use with DØ's Common Analysis Format (CAF) Environment, which is itself an extention of the high energy physics environment ROOT.

The trigger efficiency is determined by using Monte Carlo simulated events to determine whether a trigger would have fired. The Monte Carlo events are created first with an event generator such as PYTHIA [28] and the detector response to the event is simulated in GEANT [29]. The trigger requirements can now be simulated

on the Monte Carlo generated events which would, by definition of the simulated trigger, account for correlations and overlaps between the triggers. Directly simulating the trigger requirements is generally not adequate for precision measurements of the trigger efficiency. The focus of this package is to use the probabilities of a trigger to fire in data, instead of simulated events, to obtain the trigger efficiencies. These probabilities can then be used to form a trigger weight within $[0, 1]$ for each event by folding them into Monte Carlo events for a single trigger object. The total event probability can be calculated as follows

$$P(L1, L2, L3) = P(L1) \times P(L2|L1) \times P(L3|L1, L2), \tag{3.1}$$

where $P(L2|L1)$ is the conditional probability for an event to fire the L2 trigger, given that it has fired the L1 trigger. Similarly $P(L3|L1, L2)$ is the probability of an event firing the L3 trigger, given that it has fired the L1 and L2 triggers. This gives flexibility in the combination of the trigger conditions at the three trigger levels. The user can be given a total event probability for all the trigger levels or with individual probabilities for each trigger level. These probabilities are obtained assuming that the probability for a single object to satisfy a trigger condition is independent of the presence of other objects in the event. In situations where the single objects lack the correlation described, the probabilities can be reduced to a product of the probabilities for each object as in

$$P(obj_1, obj_2) = P(obj_1) \times P(obj_2), \tag{3.2}$$

where $P(obj_1, obj_2)$ is the probability of the first and second objects passing the trigger condition, which is not separable as shown if the objects are correlated. The technical methods of measuring the single object efficiencies that are used by $caf_trigger$, vary depending on whether the object is an electron, a muon or a jet. To calculate the efficiencies, these three types of objects share the need for unbiased real data samples. These data samples are then put through one of three packages which calculate the fraction of the offline reconstructed objects that satisfy the

trigger conditions: em_cert, muo_cert and $trigeff_cafe$ for electrons, muons and jets respectively.

3.2 Design and Implementation

To understand the advantages of building the package as a CAF processor, it is useful to understand the advantages of a CAF based analysis over a traditional ROOT [22] based analysis. CAF uses C++ classes which it calls processors. These processors are given a set of classes which holds the content of the root files: reconstructed objects, trigger information, object identification and detector data. Along with these objects, CAF provides a framework which automates event loops, and calls the processors for initialization, and termination of each event. There are two other useful features, of many, provided within CAF: the ability to link processors together, the ability to store information in the event loop for another processor called afterwards, and the use of a user written configuration file to specify what CAF will run and what specified values the processors will use. The value of this common framework comes from its flexibility and simplification in the implementation of an analysis; a set of code may be reconfigured and used for different tasks, and the linked processors can be reordered for different conditions. This allows for a trigger efficiency measurement, topological cuts, b-quark tagging, and many more which may use information provided by other packages through CAF.

The top level design of the package uses the concept of a chain of processors: the initialization processor, the *probability processors* and the final output processor. The probability processor will calculate the probability that a given trigger condition will pass an event. It contains the necessary combinatorics to apply the trigger condition to objects in the event. Any number of probability processors can be placed between the initialization and output processors, and their individual trigger weights can be combined as the user sees fit (see Figure 3.1).

In the first processor, cafTriggerEfficiency, an event is first searched for the physics objects that may be used in the probability calculations: electrons, muons,

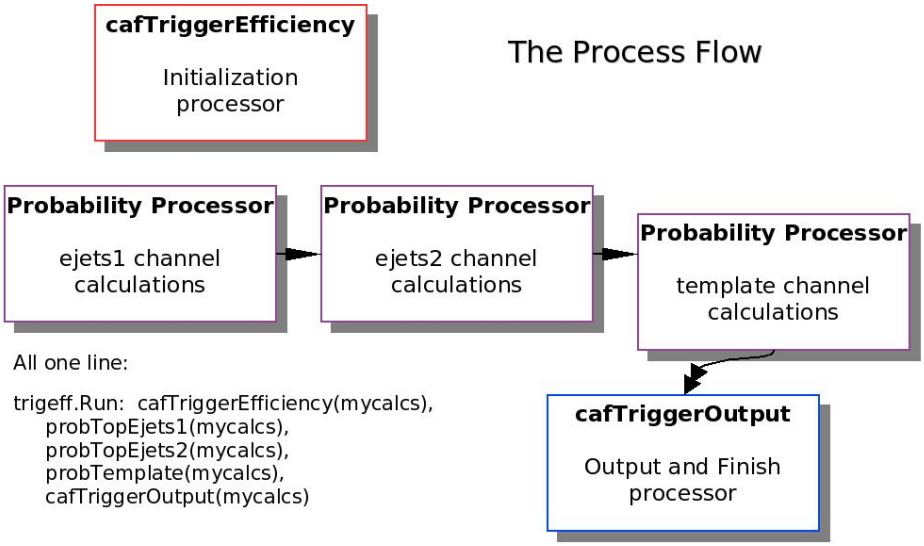

Figure 3.1: A hypothetical chain of caf_trigger processors which would produce a trigger weight for each of the three probability processors: probTopEjets1, probTopEjets2, and probTemplate.

jets and $\not\!\!E_T$, as well as the number of each of these objects. The trigger lists and their associated luminosities are also retrieved from the user specified configuration files at this time. These objects are then temporarily stored in the event being processed for the next processor in the chain, the probability processors.

3.2.1 Probability Processor

The probability processors inherit from a C++ template class which provides the writer of the processor with an interface to the turn-on curves and to the physics objects. Additionally, the base probability processor will place these objects back into the event with a specified name for further processors to use. The turn-on curves are text files which have been converted from the formats of *em_cert*, *muo_cert* and $trigeff_cafe$. These text files contain the histogrammed turn-on curves for the objects, stored in bins of variables p_T, η, and others. These text files are specified through configuration files or can be hard coded into the probability processors. The efficiencies are accessed through methods which return the values of the bins, the efficiency specified by index variable, for a given object and variable.

The main method available to the processor is one which takes as its arguments

the physics object and a variable to hold the error in the probability that is returned. This uses the text-file stored turn-on curves to return a trigger efficiency in terms of variables such as η, ϕ and p_T. The simplest use of the returned probabilities is to calculate the probability that a group of physics objects fires the trigger. As an example, if there are n muons in the event, then one could calculate the probability of that event to fire a given muon trigger by looping over the n muons in the event to obtain the probabilities for each of the n muons. One minus the total probability of none of the muons passing the trigger condition would give the overall probability for the event to fire the given trigger,

$$P(\mu) = 1 - \prod_{i=1}^{n} 1 - P(\mu_i), \tag{3.3}$$

This processor will also calculate a standard deviation, which adds or subtracts the error in the turn-on curve from its given value. Since the calculated error takes the turn-on curve and estimates an upper and lower error by moving the curve up or down by one sigma, this is a conservative estimate for the systematic uncertainty. If the probability is calculated by being split into the 3 trigger levels, the errors of the 3 levels are calculated independently so the sigma variations are added in quadrature.

There are also 4 other methods provided for each object that calculate the probability for the event to satisfy the trigger condition that X objects (where $X = 1, 2, 3, 4$) of N in the event meet a threshold requirement. These methods assume that the probability of a single object to satisfy a trigger condition is independent of other objects in the event. These are only for utility purposes since they do not calculate the correlations between the objects, and important triggers must have their own combinatorics to account for the correlations. The calculations in these methods are shown in the following equations,

$$P(X\ of\ N) = 1 - \sum_{k=1}^{X} [1 - P(only\ obj_k\ of\ N)] \tag{3.4}$$

$$1 - P(only\ obj_k\ of\ N) = (1 - P(obj_k)) \times \prod_{l=1}^{k-1} P(obj_l) \tag{3.5}$$

where $P(X\ of\ N)$ is the probability for X of N total objects to pass the trigger conditions, $P(only\ obj_k\ of\ N)$ is the probability that only object k of N total objects has passed the trigger condition, and $P(obj_k$ is the probability that object k of N has passed the trigger condition. The last definition for $P(obj_k$ is irrespective of requirements on any of the other N-1 objects. The advantage of being able to create a chain of these processors is to allow for combinatorics that would otherwise be prohibitively difficult in a single processor. It is also possible to use the several single object trigger processors with a processor at the end of the chain to combine the probability results from each processor while accounting for correlations between the triggers. Each of the processors are specified with a name denoted as a "channel" which is used as an identifier by processors that come after. This gives each processor a unique identifier for event weights that it puts into the event. The event weight and the sigma errors are then mapped to the specified channel name and passed to the next processor in the chain, which may be another probability processor or the final output processor. At the end of every event, the event weights are sorted by their channel name and by the trigger list version that had been used to calculate the weights. Each of the trigger lists are associated with a luminosity which is used to calculate an average event weight of the used trigger lists based on their luminosities.

3.2.2 The Output Processor

The final processor in the chain is the output processor, cafTriggerOutput. This processor stores, event by event, the values of the probability calculations that have been passed to it from the probability processors. These event weights are summed with the weights from previous calculations to give a total summed event weight when all events have been processed. This total weight is then divided by the number of events that have been processed to give an averaged trigger efficiency for all the events. These probability averages are displayed to the user along with

the sigma variations on the values. The event by event probabilities are also stored in histograms which aids in diagnostic of the combinatorics within a processor by showing a distribution of the event weights.

Additionally, the output processor will write the individual event weights back into the event which allows another package after *caf_trigger* to use these event weights. As an example of a simple use of this is to plot a histogram of an object and its variable before *caf_trigger* is run, and after, in order to note the changes changes to the original distributions. As an example, when studying an electron trigger, one may plot a histogram of the leading electron p_T. The event by event weights are then applied to a second histogram which is plotted after *caf_trigger* in a chain. Dividing the weighted histogram by the unweighted histogram will give a probability curve which is similar to a trigger efficiency turn-on curve. This shows how the turn-on curves will look when folded into events and so it can be used to provide a rough check of the prediction with data. It is difficult to accurately check *caf_trigger* with data because *caf_trigger* is calculating a probability for an event to pass the trigger. This is not the same as passing an event or failing an event so it will give different results when compared with a set of trigger weights where each event is passed or failed. The way to ensure that *caf_trigger* is giving sensible results is by comparison with simpler trigger efficiencies made with *caf_trigger* with combinatorics that are known to be correct, and to ensure that the turn-on curves provided by the *em_cert*, *muo_cert* and *trigeff_cafe* packages are correct. The latter can be achieved accurately through comparisons with data since they are providing a pass or fail criteria for each event to produce the turn-on curves.

Chapter 4

Electron Trigger "OR'ing"

4.1 Triggers of interest and "OR'ing"

The single top t-channel and s-channel have well defined signatures: a high energy lepton, $\not\!\!E_T$, either one b-quark jet or two b-quark jets, and possible jets from free quarks. The single top signal signature is overwhelmed by a multitude of backgrounds, the closest of which to the top signal are the $t\bar{t}$ production and the $W + jets$ background. The $W + jets$ background, may include a Wcj, Wjj, $Wb\bar{b}$ and others. In the case of the $Wb\bar{b}$ background which is prevalent in samples with 2 b-tagged jets, and it may also include a lepton and neutrino, this background cannot be decreased by just looking at the identified particles. This background will decrease as the requirement for the mass of the reconstructed top quark increases. A cut on the t-quark mass, the angular distribution of the decay particles, the particle momenta and other variables, are used to form a discriminant to reduce this background. The $t\bar{t}$ background will have the signature of a t-quark. The strategy noted earlier of looking for a lepton, $\not\!\!E_T$, and a number of jets is still useful against this background. The $t\bar{t}$ events may produce two high energy leptons (dilepton events) instead of one, and thus it is possible to reject these events by requiring only one lepton or high energy jet that has faked a lepton in the event. Such a rejection on additional "hard" jets or leptons can be loosely defined [23] as any jet or lepton with $E_T > 15 - 25$ GeV, and $|\eta| < 2.5 - 4$. If only one of the t-quarks decay leptonically, then a restriction in the number of jets can be made to further filter the sample. The samples which maximize the signal to background ratio are

$W + 2jets$ and $W + 3jets$ events, where two of the jets are from a b-quark[1].

The signature of the event as it has been described clearly indicates that an optimal trigger to use for this type of event is one which looks for an electron or muon and some jets. The focus of this trigger study is on electron triggers, the electron and jets trigger (e+Jets) and improvements that can be made to the trigger. The current trigger used is the e+Jets trigger that identifies a signal-like event based on criteria imposed on the electron and the jets in the event. The goal is to look at the improvements to the signal acceptance by first taking the OR of all the e+Jets triggers and the OR of all the single electron triggers for each trigger list. The reasoning behind this is that the single electron triggers have tighter constraints on the definition of an electron than the e+Jets triggers. In most cases, the p_T threshold of the electron triggers are higher than those of the e+Jets triggers meaning that the OR of these triggers will accept signals of the e+Jets type or electron events without the jet requirement. First, the e+Jets and single electron triggers will be defined, followed by the results of performing an OR of the triggers.

The generic definitions for the trigger terms such as $CEM(x, n)$ and $L2CALEM(n, x)$ are shown in Table (4.1) and (4.2), which also hold a glossary of terms used by the single electron triggers. The trigger list version is denoted with v8-v14. Within this table, the term "transverse shower shape (_T)" and "tight shower shape" are defined by the electromagnetic showering on each of the EM layers of the calorimeter. The EM layers are divided into 4 radial distances labelled EM1, EM2, EM3 and EM4, of which EM4 is the closest to the hadronic layers and farthest from the beam pipe. The transverse shower shape is defined as the width of the shower on the 3 EM layers, labelled EMxW. The transverse shower shape cut (_T) is defined as $EM1W < 0.09$, $EM2W < 0.08$ and $EM3W < 0.05$. This is a tighter requirement than the "tight" shower shape requirement because it is an older definition preceeding the current definitions of tight and loose. The tight shower shape requirement

[1]Although a jet may be from a b-quark, the ability to identify a b jet is based on the tracking efficiency, misreconstructed jets, the detection of jets and jets that have been incorrectly identified as jets or as other particles. These, among others, make the tagging of b jets a non-trivial exercise

Table 4.1: Glossary of L1, and L2.

Term	**Definition**
L1:	
CEM(x, n)	x Calorimeter EM trigger towers with $E_T > n\ GeV$
CJT(x, n)	x Calorimeter jet trigger towers with $E_T > n\ GeV$
ncu	Not Calorimeter Unsuppressed readout
L2:	
EM(x, n)	EM candidate with an EM fraction $> x$ and with $E_T > n\ GeV$
L2CALEM(n, x)	requires a standard EM cluster with a threshold $\geq n\ GeV$
L2CALEM(x, n, l)	requires a single EM object with isolation $< l$ and $E_T > n\ GeV$
xJET(n)	x jet candidates with $E_T > n$

is similarly defined for the CC ($EM1W < 1.8$, $EM2W < 1.4$ and $EM3W < 1.15$) and EC ($EM1W < 1.0$, $EM2W < 1.0$ and $EM3W < 1.2$) regions of the calorimeter. The loose shower shape requirement is defined for the CC ($EM1W < 2.3$, $EM2W < 1.7$ and $EM3W < 1.5$) and EC ($EM1W < 1.4$, $EM2W < 1.35$ and $EM3W < 1.4$) regions of the calorimeter. The terms LOOSE and VLOOSE electron are determined by the EM fraction, which is the faction of the energy deposited in the EM layers of the calorimeter: EM fraction > 0.9 for LOOSE, and EM fraction > 0.8 for VLOOSE. The trigger terms with *ncu* refer to hot cells in the calorimeter that would provide an incorrect measurement of the energy deposition. The requirement of the trigger is for events not using the calorimeter with unsuppressed hot cell readout.

The detailed break down of the e+Jets triggers for trigger lists v8-v14 are shown in Table (4.3) and (4.4). Generally, the e+Jets trigger requires a low p_T electron with 2 jets which may be defined with differing energies. Changes to the triggers were made over time in an attempt to improve the efficiency of the triggers with techniques such as isolation of the electron and track matching on the jets. The threshold for the electron p_T was raised at L1 as the trigger lists progressed (from

Table 4.2: Glossary of L3 terms.

Term	**Definition**
L3:	
Ele(ELE_LOOSE, x, n, 0., l)	x LOOSE electrons, $\|\eta\| < l$, with $E_T > n\ GeV$
Ele(ELE_VLOOSE, x, n, 0., l)	x VLOOSE electrons, $\|\eta\| < l$, with transverse shower shape (_T), and $E_T > n\ GeV$
Ele(ELE_LOOSE_SH_T, x, n, 0., l)	x LOOSE electrons, $\|\eta\| < l$, with transverse shower shape (_T), and $E_T > n\ GeV$
Ele(ELE_NLV, x, n, 0., l)	x LOOSE electrons, $\|\eta\| < l$, with non-linearity and vertex corrections used, with no shower shape requirements and $E_T > n\ GeV$
Ele(ELE_NLV_VL, x, n, 0., l)	x VLOOSE electrons, $\|\eta\| < l$, with non-linearity and vertex corrections used, with no shower shape requirements and $E_T > n\ GeV$
Ele(ELE_NLV_SH, x, n, 0., l)	x electrons, $\|\eta\| < l$, with non-linearity and vertex corrections used, with loose shower shape, and $E_T > n\ GeV$
Ele(ELE_NLV_SHT, x, n, 0., l)	x electrons, $\|\eta\| < l$, with non-linearity and vertex corrections used, with tight shower shape requirements, and $E_T > n\ GeV$
Ele(ELE_NLV_NC, x, n, 0., l)	x electrons, $\|\eta\| < l$, with non-linearity and vertex corrections used, and $E_T > n\ GeV$
Jet(SCJET_9, x, n)	x jets are found with $E_T > n\ GeV$ using a simple cone algorithm on jets of b GeV
Jet(SCaJET_b_PVc, x, n)	x jets with $E_T > n\ GeV$ using simple cone algorithm with cone size 0.a on jets of b GeV, and using the primary vertex tool with tracks of c GeV

Table 4.3: e+Jets triggers for trigger lists v8-v13.

v8-v11	**EM15_2JT15**
L1 all terms	CEM(1, 10)CJT(2, 5)_ncu
L2 all terms	EM(0.85, 10)_2JET(10)
L3 all terms	Ele(ELE_LOOSE_SH_T, 1, 15) _Jet(SCJET_9, 2, 15)
v12	**Ex_SHT15_2J20 (x = 1, 2, 3)**
L1 E1 terms	CEM(1, 11)_ncu
L1 E2 terms	CEM(2, 6)_ncu
L1 E3 terms	CEM(2, 3)CEM(1, 9)_ncu
L2 all terms	unrestricted trigger
L3 all terms	Ele(ELE_NLV_SHT, 1, 15) _Jet(SC5JET_9_PV3, 2, 20)
v13	**Ex_SHT15_2J_J25 (x = 1, 2, 3, 4)**
L1 E1 terms	CEM(1, 11)_ncu
L1 E2 terms	CEM(2, 6)_ncu
L1 E3 terms	CEM(2, 3)CEM(1, 9)_ncu
L1 E4 terms	CEM(1, 11)_ncu
L2 E1, E2, E3 terms	L2CALEM(15, x)
L2 E4 terms	L2CALEM(x, 11, 0.2)
L3 all terms	Ele(ELE_NLV_SHT, 1, 15.) _Jet(SC5JET_9_PV1, 2, 20.) _Jet(SC5JET_9_PV1, 1, 25.)

EM15_2JT15 to E1_2J terms), as well as changes to the jet thresholds. This was to counter the rising luminosity and was not done to improve the trigger efficiencies.

As well as the e+Jets triggers, triggering on a single electron in the event is also used, which generally trigger on a higher energy threshold than with e+Jets. The break down of the single electron triggers for trigger lists v8-v14 are shown in Table (4.5) and (4.6). The basic single electron triggers are more varied than the e+Jets triggers, which is a result of triggering only on the electron. These triggers require additional cuts to keep the trigger rates low because there is less to cut on; there is no jet requirement. The marked difference is seen at L3, as the electron triggering is similar to that of the e+Jets triggers at L1, and L2. At L3, the electron requirements for the e+Jets trigger have a threshold at electron $p_T >$ 15 GeV/c, whereas the single electron trigger varies from a 20 GeV/c threshold

Table 4.4: e+Jets triggers for trigger lists v13.3-v14.

v13.3	**Ex_SHT15_2J_J30 (x = 1, 2, 3, 4)**
L1 E1 terms	CEM(1, 11)_ncu
L1 E2 terms	CEM(2, 6)_ncu
L1 E3 terms	CEM(2, 3)CEM(1, 9)_ncu
L1 E4 terms	CEM(1, 11)_ncu
L2 E1, E2, E3 terms	L2CALEM(15, x)
L2 E4 terms	L2CALEM(x, 11, 0.2)
L3 all terms	Ele(ELE_NLV_SHT, 1, 15.) _Jet(SC5JET_9_PV1, 2, 20.) _Jet(SC5JET_9_PV1, 1, 30.)
v14	**Ex_SHT15_2J_J30 (x = 1, 3, 4)**
L1 E1 terms	CEM(1, 12)_ncu
L1 E3 terms	CEM(2, 3)CEM(1, 9)_ncu
L1 E4 terms	CEM(2, 6)_ncu
L2 all terms	L2CALEM(15, x)
L3 all terms	Ele(ELE_NLV_SHT, 1, 15.) _Jet(SC5JET_9_PV3, 2, 20.) _Jet(SC5JET_9_PV3, 1, 25.)

to one at 90 GeV/c. The difference is in the cuts applied to the shape of the EM shower, and the EM fraction. The single electron triggers have a more efficient event acceptance for high energy electrons, although it may reject single top events. This is because the triggers have no requirements on the jets and a higher requirement on the electron. Single top events with the required jets but with a lower electron p_T than required may be rejected.

The single electron triggers are high p_T electron triggers which have a good efficiency for high p_T events like single top. The e+Jets triggers have a low p_T threshold which includes a jet requirement. The lower requirements lead to lower efficiencies due to the high background rates compared to the signal events. Taking the OR of one with the other should provide a higher acceptance for our signal. Given two triggers, T_A and T_B, the combination of firing can occur in four ways: T_A and T_B both fire, T_A fires but not T_B, T_B fires but not T_A, and neither T_A nor T_B fire. This shows, through a simple Venn diagram, the following probability equation

Table 4.5: Single electron triggers for trigger lists v8-v13.

v8-v11	**EM_MX, EM_MX_SH, EM_MX_EMFR8, EM_HI, EM_HI_SH, EM_HI_EMFR8**
L1 EM_MX terms	CEM(1, 15)_ncu
L1 EM_HI terms	CEM(1, 10)_ncu
L2 all terms	unrestricted trigger
L3 EM_(MX/HI)	Ele(ELE_LOOSE, 1, 30. ,0. , 3.)
L3 EM_(MX/HI)_SH	Ele(ELE_LOOSE_SH_T, 1, 20., 0., 3.)
L3 EM_(MX/HI)_EMFR8	Ele(ELE_VLOOSE,1,40.,0.,3.)
v12	**Ex_SHT20, Ex_SH30, E1_L50, E1_VL70 (x = 1, 2, 3)**
L1 E1 terms	CEM(1, 11)_ncu
L1 E2 terms	CEM(2, 6)_ncu
L1 E3 terms	CEM(2,3)CEM(1,9)_ncu
L2 all terms	unrestricted trigger
L3 Ex_SHT20 (x = 1, 2, 3)	Ele(ELE_NLV_SHT, 1, 20., 0., 3.6)
L3 Ex_SH30 (x = 1, 2, 3)	Ele(ELE_NLV_SH, 1, 30., 0., 3.6)
L3 E1_L50	Ele(ELE_NLV, 1, 50., 0., 3.6)
L3 E1_VL70	Ele(ELE_NLV_VL, 1, 70., 0., 3.6)
v13	**Ex_SHT20, Ex_SH30, E1_L50, E1_NC90 (x = 1, 2, 3, 4)**
L1 E1 terms	CEM(1, 11)_ncu
L1 E2 terms	CEM(2, 6)_ncu
L1 E3 terms	CEM(2, 3)CEM(1, 9)_ncu
L1 E4 terms	CEM(1, 11)_ncu
L2 E1, E2, E3 terms	L2CALEM(15, x)
L2 E4 terms	L2CALEM(x, 11, 0.2)
L3 Ex_SHT20 (x = 1, 2, 3, 4)	Ele(ELE_NLV_SHT, 1, 20., 0., 3.6)
L3 Ex_SH30 (x = 1, 2, 3, 4)	Ele(ELE_NLV_SH, 1, 30., 0., 3.6)
L3 E1_L50	Ele(ELE_NLV, 1, 50., 0., 3.6)
L3 E1_NC90	Ele(ELE_NLV_NC, 1, 90., 0., 3.6)

Table 4.6: Single electron triggers for trigger lists v13.2-v14.

v13.2	**Ex_SHT22, Ex_SH30, E1_L70, E1_NC90 (x = 1, 2, 3, 4)**
L1 E1 terms	CEM(1, 11)_ncu
L1 E2 terms	CEM(2, 6)_ncu
L1 E3 terms	CEM(2, 3)CEM(1, 9)_ncu
L1 E4 terms	CEM(1, 11)_ncu
L2 E1, E2, E3 terms	L2CALEM(15, x)
L2 E4 terms	L2CALEM(x, 11, 0.2)
L3 Ex_SHT22 (x = 1, 2, 3, 4)	Ele(ELE_NLV_SHT, 1, 22., 0., 3.6)
L3 Ex_SH30 (x = 1, 2, 3, 4)	Ele(ELE_NLV_SH, 1, 30., 0., 3.6)
L3 E1_L50	Ele(ELE_NLV, 1, 50., 0., 3.6)
L3 E1_NC90	Ele(ELE_NLV_NC, 1, 90., 0., 3.6)
v14	**Ex_SHT25, Ex_SH35, E1_L70 (x = 1, 3, 4)**
L1 E1, E3 terms	CEM(1, 12)_ncu
L1 E4 terms	CEM(2, 6)_ncu
L2 E1, E4 terms	L2CALEM(15, x)
L2 E3 terms	L2CALEM(x, 11, 0.2)
L3 Ex_SHT25 (x = 1, 3, 4)	Ele(ELE_NLV_SHT, 1, 25., 0., 3.6)
L3 Ex_SH35 (x = 1, 3, 4)	Ele(ELE_NLV_SH, 1, 35., 0., 3.6)
L3 E1_L70	Ele(ELE_NLV, 1, 70., 0., 3.6)

$$P(T_A \vee T_B) = P(T_A) + P(T_B) - P(T_A \wedge T_B). \tag{4.1}$$

where $P(T_A)$ is the probability of T_A firing, $(T_A \vee T_B)$ means (T_A or T_B), and $(T_A \wedge T_B)$ means (T_A and T_B). Table (4.3) and (4.4) show that the electron trigger criteria is varied while the jet criteria remain constant within each trigger list. So, for a given trigger list, the probability of the e+Jets trigger may be factored out into its component pieces. Let $P(E_S)$ be the probability of an event passing the single electron criteria, EJ be the probability of an event passing the e+Jets trigger criteria, E_{EJ} be the electron criteria of the e+Jets trigger, and J_{EJ} be the jets criteria of the e+Jets trigger. Then the probability of $E_S \vee EJ$ is given by

$$P(E_S \vee EJ) = P(E_S) + P(E_{EJ}) \times P(J_{EJ}) - P(E_S \wedge E_{EJ}) \times P(J_{EJ}). \tag{4.2}$$

The equation shows that $P(E_S \vee EJ)$ does not equate to the simple quantity $P(E_S \vee E_{EJ}) \times P(J_{EJ})$, because there are correlations between the electron triggers that must be taken into account. Due to the abundance of the words "OR" and "AND", I will be using the notation ($X^{OR} = X^1 \vee X^2 \vee ...$), defined to be the OR of triggers (X^1, $X^2, ...$). Each of the quantities on the right hand side of Equation (4.2) can be calculated: the trigger turn-on curves will first be produced in the *em_cert* [24] package for the OR's of the single electron triggers ($E_S^{OR} = E_S^1 \vee E_S^2 \vee ...$), the OR's of the electron portion of the e+Jets triggers ($E_{EJ}^{OR} = E_{EJ}^1 \vee E_{EJ}^2 \vee ...$), and the AND's of all these triggers ($E_S^{OR} \wedge E_{EJ}^{OR}$). These will be combined with jet turn-on curves produced with the $trigeff_cafe$ [25] package.

The trigger efficiencies are not so easily handled when the triggers are prescaled. To prescale a trigger is to set a limit on the number of trigger accepts that are stored. This is normally done with a simple condition such as "keep 1 in 300 accepts", and is performed at higher luminosities to lower the acceptance rate to keep within the trigger bandwidth. The triggers studied were not prescaled, although the normalization when combining triggers is accounted for in the *em_cert* and

$trigeff_cafe$ packages since they apply the trigger conditions directly to the data. The processor created in $caf_trigger$ to calculate the OR of the triggers was created with the future intention of using prescaled triggers with the method shown in reference [26], but this feature was not used for the results presented here.

4.2 The Turn-on Curves

The turn-on curves for the electron and jet portion of the triggers are created in two seperate packages: em_cert and $trigeff_cafe$. Ideally, one is interested in calculating the trigger efficiency and producing a turn-on curve by testing a desired object against a trigger as follows,

$$Eff = \frac{Events_{pass\ trigger}}{Events_{all}}. \tag{4.3}$$

All events that have been recorded during data taking must pass one or more triggers. This introduces a bias to the efficiency calculation as events that were accepted by a certain trigger will be seen as an efficiency of 1.0. As an example, recorded events that pass an electron trigger with the requirement $p_T > 20$ GeV/c are very likely to pass an electron requirement of $p_T > 10$ GeV/c, which would make any studies of the later trigger meaningless. Further, trigger conditions vary from requiring track matches to requiring an amount of energy in the calorimeter and may then bias other triggers with similar requirements.

The em_cert package uses a method to minimize the trigger bias known as tag and probe. The goal of this method is to identify events in which the electrons reconstruct to a Z boson. The first step is to look at events with at least two good EM clusters that reconstruct into a Z which may be used as the tag and probe electrons. This is done by requiring that the invariant mass of the tag and probe electrons sits between 65 GeV/c^2 and 200 GeV/c^2. At least one of the two EM clusters are required to have a $E_T > 25$ GeV and matched to a track within the detector, which we shall call $em1$. The second EM cluster, $em2$, is required to be matched to an isolated track. $em1$ must now pass a few conditions before it is

accepted as a tag: the first is a likelihood cut for the electron, and the second is a requirement that $em1$ passes any of the electron triggers. The likelihood cut is a cut on the probability that the identified object is an electron, which is constructed with various requirements for the electron. If these requirements are filled, $em2$ is taken as the probe and is tested against every electron trigger and a histogram is filled if it passes the trigger condition

$$Eff_{withvalidtag} = \frac{Probe_{pass\ trigger}}{Probe_{all}}, \tag{4.4}$$

where the histogram is filled if the event has a valid tag and the ratio is taken of the events with a probe passing the trigger to all events with a valid tag. After $em2$ has been tested, the roles of the two EM clusters switch. The process begins again with the requirement that the two good EM clusters reconstruct into a Z. $em2$ is now put through the same conditions to be a tag electron. For those events that have $em2$ as a tag, $em1$ becomes the probe and is tested against the electron triggers and those that pass are used to fill the same histogram. Depending on the methods used in the selection of the tag electron, there may arise correlations between the tag and probe objects. As an example, the efficiency could be dependent on the primary vertex position [24]. The selection of the tag electron could bias the vertex distribution which would bias the probe electron identification efficiency. These biases can be removed with an understanding of the selection methods used for the tag and probe objects.

While the tag and probe method is applicable to jets, it is not the method that was used in $trigeff_cafe$. This is because the method would require a Z decaying into two quarks to produce the jets for the reconstruction. Due to the high background production of jets, it is not a clean signal of the Z like with leptons and so $trigeff_cafe$ must rely on another method to ensure an unbiased sample. The trigger bias, in this case, is removed by a selection criteria on the data events. The events used to calculate the trigger efficiency are chosen by only including events that have been accepted by selected muon triggers which do not make use

of calorimeter information because the jet triggers will use deposited calorimeter energy. The trigger efficiency is then calculated, after the selection of the required data, through a simple ratio

$$Eff_{with\ muon\ trigger} = \frac{good\ jets\ \&\ Events_{pass\ trigger}}{good\ jets\ \&\ Events_{all}}, \tag{4.5}$$

where a good jet is defined by a set of quality cuts such as energy deposited in the calorimeter and electron vetos. There is one more set of turn-on curves that is relevant to the calculation, and that is the correlation of an electron object with a jet object. This arises through a calculation of the efficiency for an electron, which has passed the electron trigger conditions, to fire a jet trigger. This is referred to as the SCJET efficiency and as EM shaping of the jets at L3. The efficiency is calculated within *em_cert* by taking the events which have passed the electron trigger of interest, and seeing if these events pass a jet trigger condition. This is done at various thresholds of the jet p_T (15, 20, 25, 30, and 35 GeV/c) in the following equation:

$$Eff_{SCJET} = \frac{Events_{pass\ electron\ trigger}\ \&\ Events^{threshold}_{pass\ jet\ trigger}}{Events_{pass\ electron\ trigger}}, \tag{4.6}$$

where $Events_{pass\ electron\ trigger}$ are the events that pass the electron trigger criteria and $Events^{threshold}_{pass\ jet\ trigger}$ are the events that pass the jet criteria at a specified threshold. The SCJET turn-on curves are used in *caf_trigger* to produce a trigger efficiency for $P(E_{EJ}) \times P(J_{EJ})$ and for $P(E_S \wedge E_{EJ}) \times P(J_{EJ})$. A representative plot of these turn-on curves can be seen in Figure (4.1). The turn-on curves were only produced for $p_T = 20, 25, 30 and 35$ GeV/c and it has been assumed that for a threshold of $p_T = 15\ GeV$, the correlation of the SCJET and electron triggers is 100%. Since the v8-v11 trigger lists used an L3 trigger term of $Ele(ELE_LOOSE_SH_T, 1, 15)_Jet(SCJET_9, 2, 15)$ (Table (4.3)), which has a p_T threshold of 15 GeV/c, SCJET turn-on curves were unnecessary.

The *em_cert* package was run on data events which have either two electrons with $p_T > 12$ GeV/c, or two tracks which are associated with reconstructed electrons.

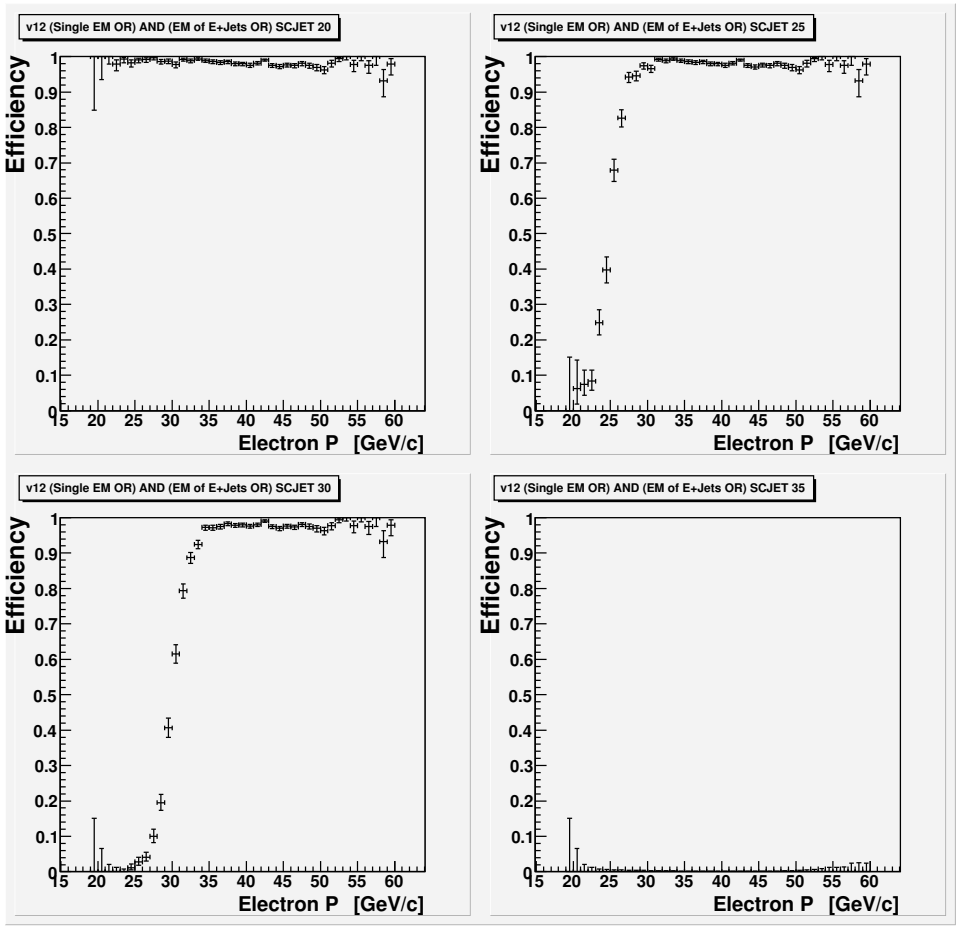

Figure 4.1: The turn-on curve for the v12 electron triggers firing a jet trigger, $(Ex_SHT20 \vee Ex_SH30 \vee E1_L50 \vee E1_VL70) \wedge Ex_SHT15 \wedge SCJET(y)$, where x = 1, 2, 3 and y = p_T threshold of 20, 25, 30 and 35 GeV/c. The turn-on curves for the other trigger lists can be found in Appendix A.

The *trigeff_cafe* package was run on data events with a non-calorimeter muon trigger. Both of these packages ran on data which has been reconstructed with the DØ reconstruction program DØReco version p17.09.03: *em_cert* on a subset of the data with 2 electrons with high p_T (CSskim-2EMhighpt-PASS3-p17.09.03), and *trigeff_cafe* on a similar skim of the data with jets (CSskim-TOPJETTRIG-PASS3-p17.09.03) [27]. The turn-on curves output from *em_cert* is shown in Appendix A, while the turn-on curves output from *trigeff_cafe* were created by Thomas Gadfort so the direct output before the conversion to a text format is unavailable.

The turn-on curves are produced in the form of histograms of the efficiencies, defined in Equation (4.3), binned in variables of p_T, η, and others. Ideal turn-on curves of single trigger, single object efficiencies are step functions at the threshold that has been set. In practice, the resolution of the detector smears measurements of a value to a Gaussian distribution. Since the trigger efficiency is a convolution of this gaussian distribution with the step function efficiency curve, the turn-on curves in p_T can be fitted to an error function of the form

$$f(x) = \frac{A_2}{2}\left(1 + \mathrm{Erf}\left(\frac{p_T - A_0}{\sqrt{2}A_1}\right)\right), \tag{4.7}$$

where Erf() is an error function, A_0 is the midpoint, A_1 is the slope and A_2 is the plateau of the turn-on curve. The use of OR'd triggers precludes the use of this fit as the turn-on curves are no longer those of a single trigger. This means that the turn-on curve will be a combination of more than one error function which cannot be fitted to a single error function. A clear example of this can be seen in Figure (4.2) which shows two plateaux after the "turn-on": one with $26 < p_T < 32$ GeV/c and the other with $p_T > 32$ GeV/c. Although the single triggers can be fitted to an error function, they were not fitted for consistency with the OR'd triggers.

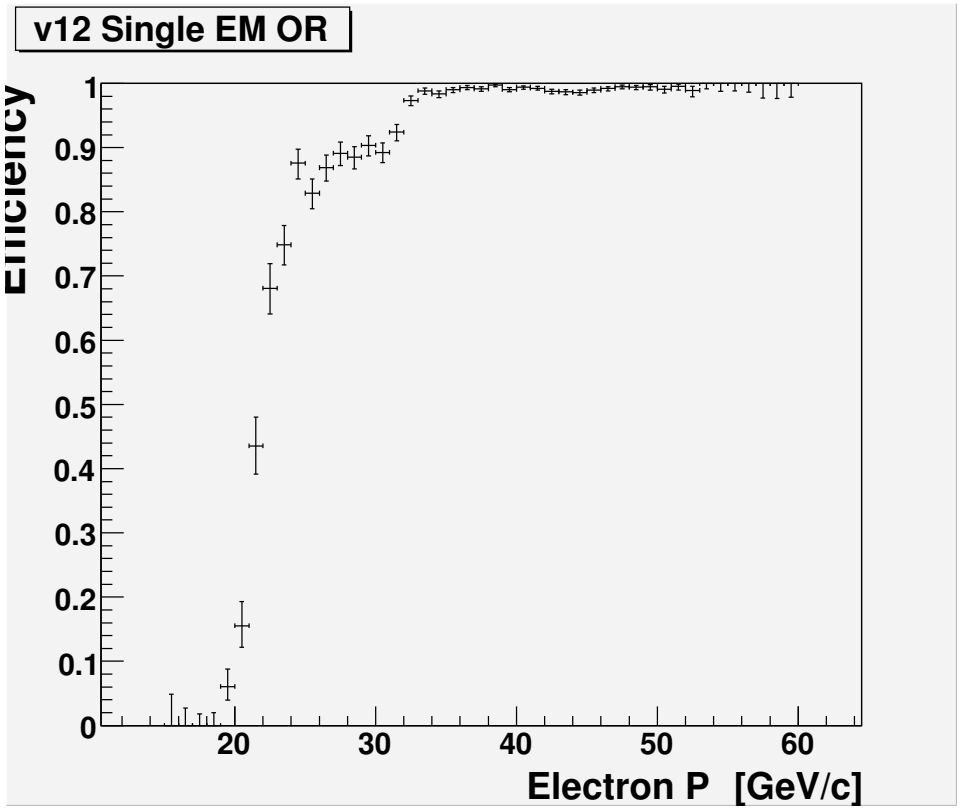

Figure 4.2: The turn-on curve for the v12 single electron triggers, $Ex_SHT20 \vee Ex_SH30 \vee E1_L50 \vee E1_VL70$, where x = 1, 2, 3 (Table (4.5)). The turn-on curves for the other trigger lists are in Appendix A.

4.3 Trigger Efficiencies in caf_trigger

4.3.1 The Single Electron, and e+Jets Triggers

Probability processors with the combinatorics to calculate the single electron, e+Jets, and single electron $\wedge$ e+Jets efficiencies are used in *caf_trigger* to calculate the efficiencies for single electron $\vee$ e+Jets. This is done with 4 processors: the single electron processor using the E_S turn-on curves, the e+Jets processor using the E_{EJ} and J_{EJ} turn-on curves, the e+Jets processor using the $E_S \wedge E_{EJ}$ and J_{EJ} turn-on curves, and a final combination processor.

The combinatorics of the single electron trigger use the combined L1, L2, and L3 turn-on curves produced in *em_cert*. The combinatorics involved were discussed in chapter 3, giving a probability for the event to fire an electron trigger with the assumption that the electrons in the event are independent. The probability of each electron, with a given p_T, not to fire the given trigger is calculated. These are then multiplied together to obtain the the probability of all of the electrons not to fire the trigger, which is subtracted from 1 to give the probability of the electrons firing the trigger.

$$P(E_S) = 1 - \prod_{i=1}^{n} 1 - P(e_i). \tag{4.8}$$

The combinatorics of the e+Jets trigger is factored into two pieces: the electron probability and the jet probability. The electron probability and the jet probability are calculated separately with the ability to use the OR'd triggers or the single trigger efficiencies for the electron probability calculations. These are then multiplied together to get the total e+Jets trigger efficiency.

The electron probability is calculated in the same method as the single electron probability but with the e+Jets combined L1, L2, and L3 turn-on curves for the electron (E_{EJ}). The jet probability is calculated using individual L1, L2, and L3 turn-on curves for trigger lists v8-v11, and only an L3 turn-on curve for trigger lists v12-v14. This was split in such a way to allow for the combined L3 turn-on curves provided by *em_cert* to be used with similar turn-on curves provided

by $trigeff_cafe$. The probabilities are first split by trigger list and then by p_T thresholds of the condition for firing the trigger: 15, 20, 25, and 30 GeV/c. This is done in order to include the probabilities for an electron to fake a jet at the various thresholds that are used by the e+Jets trigger. The p_T threshold at 35 GeV/c is not used since it is not in any of the current e+Jets triggers (up to $p_T = 30$ GeV/c in trigger list v13.3). Of the listed thresholds, up to 3 of them will be used for an e+Jets trigger condition, but the remaining threshold is available for ease of use. The probabilities for jet objects to fire jet trigger conditions are calculated with the added probabilities from electrons faking jets in the event. These are then split into the same p_T thresholds as for the electron and treated as probabilities for the jet to fire the jet trigger.

This can be seen more clearly with a look at the procedure of a probability calculation. The v12-v14 trigger lists have two jet criteria set at one threshold X and Y, where $X = Y$ (v12) or two different thresholds X and Y, where $X > Y$ (v13-v14). This sets a criteria for at least one of the "jets" to have $E_T > X$ GeV and at least one more jet with $E_T > Y$ GeV, where "jets" refer to objects that have satisfied the jet criteria but may be another particle like an electron. Two calculations are made:

$$P_1(L3) = \prod_{i=1}^{n} \left[1 - P_X^{L3}(jet_i)\right], \tag{4.9}$$

$$P_2(L3) = \sum_{i=1}^{n} \left[P_X^{L3}(jet_i) \prod_{j=1, i\neq j}^{n} \left(1 - P_Y^{L3}(jet_j)\right)\right]. \tag{4.10}$$

$P_X^{L3}(jet_i)$ and $P_Y^{L3}(jet_j)$ are the probabilities for a jet at level 3 to have $E_T > X$ or $> Y$ GeV, n = the number of true jets + the number of electrons, jet_i is the ith jet object, $P_1(L3)$ is a calculation that none of the "jets" have $E_T > X$ GeV, and $P_2(L3)$ is a calculation that at most one of the "jets" has $E_T > X$ GeV and there are no other "jets" with $E_T > Y$ GeV, where $X > Y$. The probability to fire the trigger is

$$P(J_{EJ}) = 1 - P_1(L3) - P_2(L3), \tag{4.11}$$

which calculates the probability for at least one of the "jets" to be above X GeV, added to the probability of at most one "jet" to be below X GeV while at least one "jet" is above Y GeV.

Equation (4.9) to (4.11) require a slight modification for use with the v8-v11 trigger lists, since these trigger lists used seperate L1, L2, and L3 trigger turn-on curves. As with the v12 trigger list, the trigger criteria requires 2 jets above a set threshold which sets $X = Y$ in Equation (4.10). Equation (4.9) is also modified to the following,

$$P_1(L1) = \prod_{i=1}^{n} \left[1 - P_X^{L1}(jet_i)\right], \text{ and } P_1(L2) = \prod_{i=1}^{n} \left[1 - P_X^{L2}(jet_i)\right], \tag{4.12}$$

where P_1L1 and P_1L2 are the probabilities that none of the "jets" fire the level 1 and level 2 trigger criteria for the threshold of 15 GeV. The probability to fire the trigger for v8-v11 trigger lists is calculated using

$$P(J_{EJ}) = (1 - P_1(L1)) \times (1 - P_1(L2)) \times [1 - P_1(L3) - P_2(L3))], \tag{4.13}$$

The jet calculations together with $P(E_{EJ})$ produce the quantity $P(E_{EJ}) \times P(J_{EJ})$, required for the final trigger OR'ing. The last calculation uses the e+Jets probability processor with the OR'd triggers, $E_S \wedge E_{EJ}$, for the electron portion and the regular jet turn-on curves for the jet portion. This produces the final value, $P(E_S \wedge E_{EJ}) \times P(J_{EJ})$, needed to produce $P(E_S \vee EJ)$. Once the three processors ($P(E_S)$, $P(E_{EJ}) \times P(J_{EJ})$, and $P(E_S \wedge E_{EJ}) \times P(J_{EJ})$) have completed their calculations in the event, these event weighting probability values are sent to a combination processor. The combination processor calculates the probability that the event fired the trigger $E_S \vee EJ$ by using Equation (4.2).

Once the three processors ($P(E_S)$, $P(E_{EJ})\times P(J_{EJ})$, and $P(E_S \wedge E_{EJ})\times P(J_{EJ})$) have completed their calculations in the event, these event weighting probability values are sent to a combination processor. The combination processor calculates the probability that the event fired the trigger $E_S \vee EJ$ by using Equation (4.2).

4.3.2 "OR'ing" and Results

The e+Jets triggers, used by the top analysis group for their efficiency calculations, are EM15_2JT15 for v8-v11, E1_SHT15_2J20 for the v12, E1_SHT15_2J_J25 for v13, and E1_SHT15_2J_J30 for the v13.3-v14 trigger lists and shall be referred to as the "main e+Jets triggers". Since the e+Jets turn-on curves produced for their calculations were fitted to an error function (Equation (4.7)), a comparison with the current unfitted turn-on curves used in the trigger ORing required new unfitted turn-on curves for the main e+Jets triggers in order to gauge the resulting OR. This was done to avoid comparing efficiencies from error function fitted histograms to unfitted histograms. The unfitted main e+Jets turn-on curves were used in a chain of *caf_trigger* processors: the 3 processors required for the OR'ing, the combination processor, and the unfitted main e+Jets calculation.

caf_trigger runs at the end of a chain of processes that are used during analysis to ensure good quality data. Only a few of these processes will remove a significant, tens of percents, of the total number of events: removal of events which are not of good data quality, a duplicate event finder, a cut on good electrons, a jet selection algorithm, and a triangle cut on $\not{E}_T$ and electron p_T. An event can be tagged as one which is not of good data quality based on many different criteria, a few of which are: the proton/anti-proton beam is noisy, detector miscalibration, hot cells in the calorimeter which register false hits, and others. The cuts on good electrons are defined by the energy deposition in the calorimeter and how well an electron matches to a track. The jet selection algorithm defines a jet cone to ensure that the object is a jet and not a misidentified particle, ensure that it matches to a track, and other criteria. The triangle cut is a topological cut used to ensure that the $\not{E}_T$ calculated in the event is valid kinematically. These processes remove

Table 4.7: Trigger lists and associated luminosities

Trigger List	v8	v9	v10	v11	v12	v13.0	v13.3	v14
Luminosity (pb^{-1})	4.21	21.42	8.48	54.32	195.29	46.77	263.98	211.19

events before *caf_trigger* or any analysis is performed, and have been included in order to produce the trigger efficiencies for the events that are used for the final analysis. The two sets of Monte-Carlo examined are *tb*-eνbb (electron, neutrino and 2 *b*-quarks) and *tqb*-eνbqb (electron, neutrino, 2 *b*-quarks and another light quark) single top events that were produced in a custom implementation of CompHEP [30] known as SingleTop [31]. These create parton-level events are then processed in PYTHIA [28] and EVTGEN [32]. These are then processed with a full GEANT [29] simulation of the DØ detector. The *tb* and *tqb* MC sets contain 92620 and 130068 events respectively. These are reduced to 41233 (*tb*) and 52715 (*tqb*) by the electron and jet selections, and further reduced to 35346 (*tb*) and 46058 (*tqb*) events by the topological cuts.

The luminosity numbers used for each trigger list, shown in Table (4.7), are from data skims which are defined with a number of cuts: one jet with $E_T > 15$ GeV and detector $|\eta| < 2.5$, one loose EM object with $p_T > 15$ GeV, $\not\!\!E_T > 15$ GeV, good data quality, and finally the e+Jets trigger. These come from the luminosity block, which is the fundamental unit of time for the luminosity measurement. These blocks are indexed by a luminosity block number which is incremented during the run. The luminosity is then calculated independently for each block [33]. These numbers are used to weight the trigger lists within *caf_trigger* in order to produce the correct luminosity averaged trigger efficiency.

The single electron OR'd triggers have significantly different turn-ons than the e+Jets OR'd triggers, arising from the higher thresholds for the acceptance of an electron in the event. The probability distribution in p_T of the leading electron for $P(E_S)$, $P(E_{EJ}) \times P(J_{EJ})$, and $P(E_S \wedge E_{EJ}) \times P(J_{EJ})$ are shown in Figure (4.3) for the *tb* and *tqb* MC. These are combined on an event by event basis to form the final

Table 4.8: Luminosity weighted $E_S \vee EJ$ vs original e+Jets trigger efficiencies, for the leading electron, of the *tb*-eνbb and *tqb*-eνbqb MC with trigger lists v8-v14.

tb $E_S \vee EJ$	$89.9 \pm^{1.0}_{0.7}$ %
tb e+Jets original	$83.6 \pm^{0.6}_{0.5}$%
tqb $E_S \vee EJ$	$89.5 \pm^{1.0}_{0.9}$ %
tqb e+Jets original	$82.2 \pm^{0.6}_{0.6}$%

Table 4.9: $E_S \vee EJ$ vs original e+Jets trigger efficiencies, for the leading electron, of the *tb*-eνbb and *tqb*-eνbqb MC vs trigger list. Trigger lists v8-v11 have been combined since there are no changes to the triggers during that period.

Trigger List	v8-v11	v12	v13.0	v13.3	v14
tb $E_S \vee EJ$	91.1%	89.9%	90.6%	90.3%	88.7%
tb e+Jets original	89.9%	82.8%	83.5%	82.8%	82.6%
tqb $E_S \vee EJ$	90.9%	89.6%	90.2%	89.8%	88.4%
tqb e+Jets original	89.4%	81.3%	82.0%	81.0%	81.1%

$P(E_S \vee E_{EJ}) \times P(J_{EJ})$ seen in Figure (4.4). Although the single electron trigger has a visually higher efficiency in the graphs, the e+Jets trigger has the actual advantage numerically: $84.1 \pm^{0.6}_{0.5}$% *tb* MC and $82.7 \pm^{0.6}_{0.6}$% *tqb* MC for the OR'd e+Jets triggers and $81.7 \pm^{0.4}_{0.2}$% *tb* MC and $81.1 \pm^{0.4}_{0.2}$% *tqb* MC for the OR'd single electron triggers. The luminosity averaged trigger efficiencies, for trigger lists v8-v14, are shown in Table (4.8). The $E_S \vee EJ$ trigger show an overall gain of $6.3 \pm^{1.2}_{0.9}$% for the *tb* MC, and $7.3 \pm^{1.2}_{1.1}$% for the *tqb* MC.

It is informative to look at the trigger efficiencies for the individual trigger lists which are shown in Table (4.9) for the *tb* and *tqb* MC. The production of uncertainties for the individual trigger lists would be computationally consuming and would not provide any further information as they are of the same order of magnitude as for the full set of trigger lists. The gains for trigger lists v8-v11 are minimal compared with the later trigger lists but the efficiencies of the e+Jets triggers before calculating the OR'd results are already near 90% efficiency.

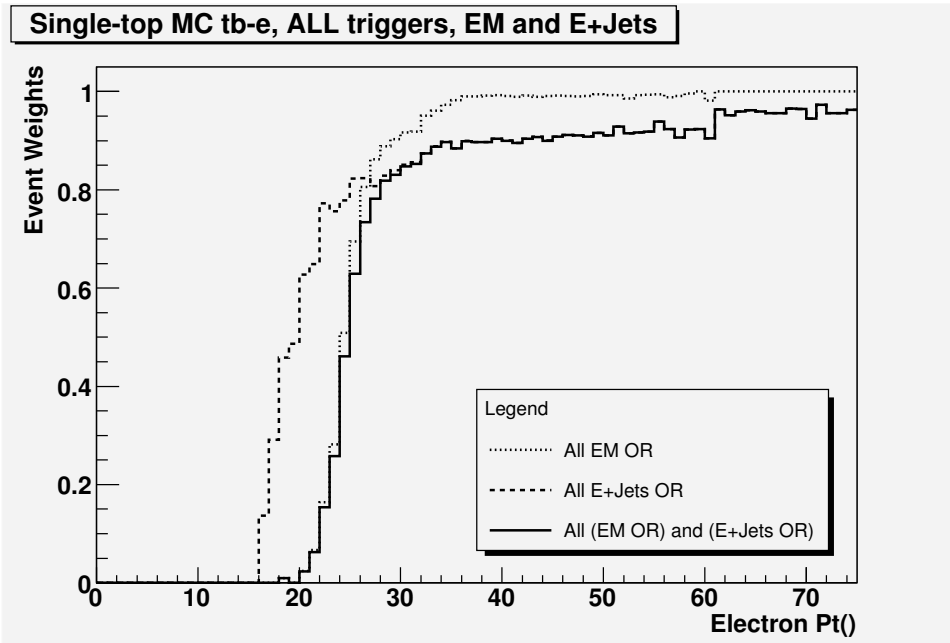

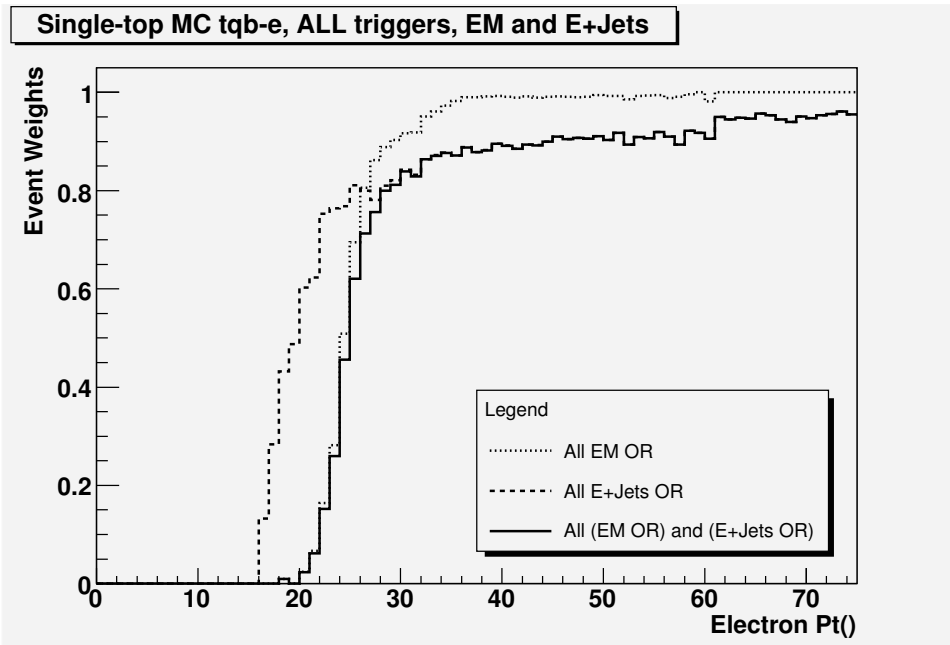

Figure 4.3: $P(E_S)$, $P(E_{EJ}) \times P(J_{EJ})$, and $P(E_S \wedge E_{EJ}) \times P(J_{EJ})$ trigger probability distribution in p_T for the leading electron.

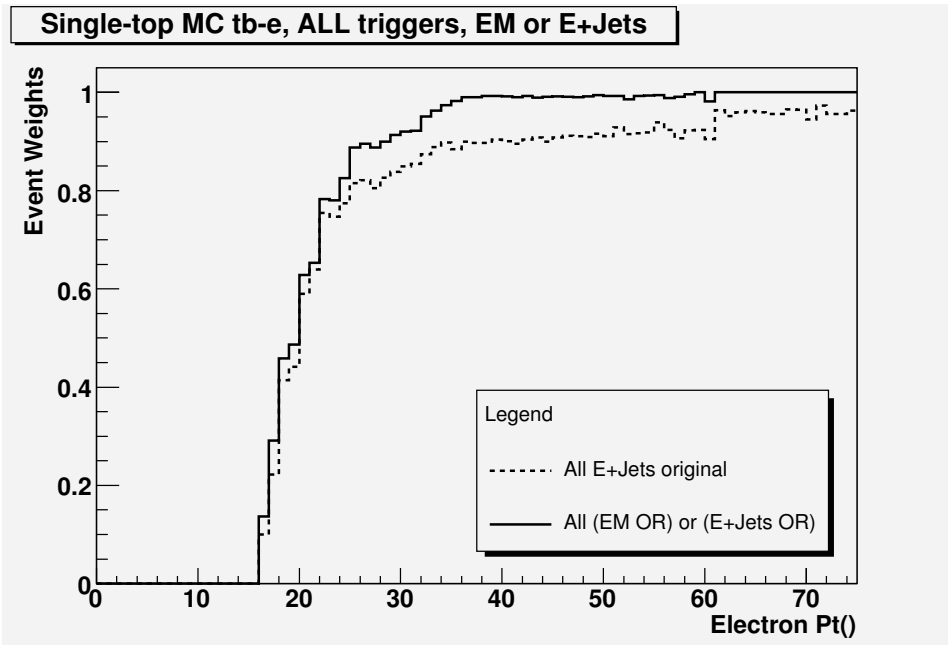

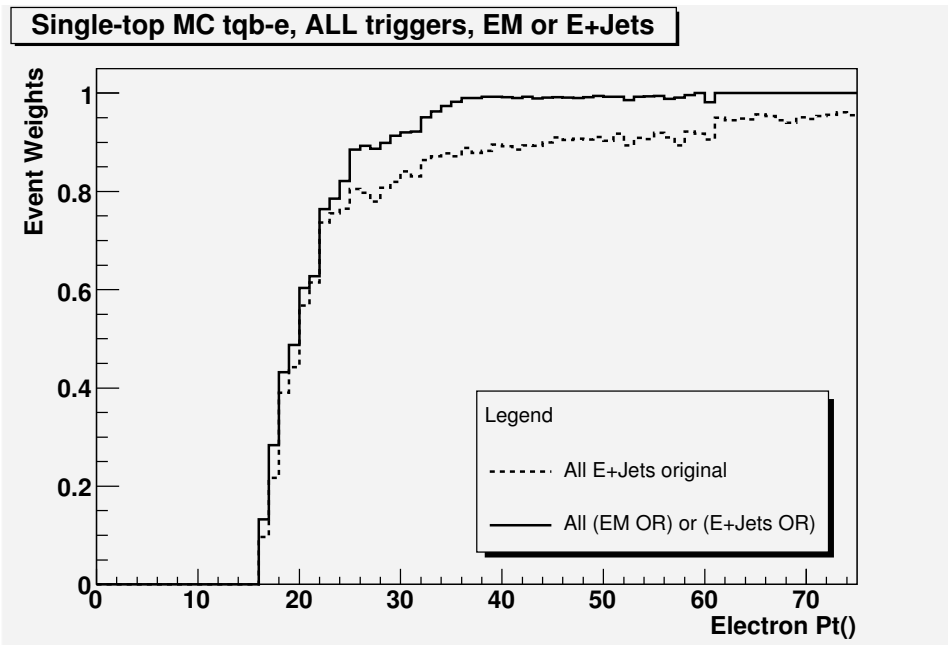

Figure 4.4: $E_S \vee EJ$ vs original e+Jets trigger probability distribution in p_T for the leading electron.

Chapter 5

Conclusions

The goal of this study was to look at increasing the efficiency of the triggers used in the analysis of the single top event signal. Towards this end, a general framework for trigger studies was created called *caf_trigger*. The *caf_trigger* package which was created for the purpose of folding trigger efficiencies derived from unbiased data to Monte-Carlo simulated events in order to produce a probability for the signal events to pass the given triggers. *caf_trigger* is now used by the DØ collaboration for trigger efficiency studies in many different analyses and was recently used for the single top analysis in 2007.

Trigger turn-on curves were created in the *em_cert* package of a logical OR of the single electron triggers, a logical OR of the E+Jets triggers, and the AND of these two trigger groups, which were to be used in *caf_trigger*. The turn-on curves for the original E+Jets triggers used in the single top analysis were also produced and used in *caf_trigger*. The luminosity weighted average of the trigger efficiencies was produced for trigger lists v8-v14 which were then compared to the original E+Jets triggers. This showed an overall gain of $6.3\pm^{1.2}_{0.9}\%$ for the *tb* MC, and $7.3\pm^{1.2}_{1.1}\%$ for the *tqb* MC in efficiency, which is a gain of $6.9\pm^{1.2}_{1.0}\%$ in efficiency for the combined *tb* and *tqb* MC.

A conservative estimate can be made of the gain in the significance of the signal by considering one of the backgrounds to the signal. The two main backgrounds are the $W + Jets$ background and the $t\bar{t}$ background. We consider the $t\bar{t}$ background in which one of the W bosons decays leptonically and the other decays to two light

quarks. Unlike the $W + Jets$ background, the $t\bar{t}$ background will have an event signature that contains two top quarks and should have a high trigger efficiency with the OR'd triggers under consideration. An estimate of the significance can be calculated by assuming a Gaussian uncertainty on the background

$$\text{gain}_{\text{significance}} = \frac{\text{gain}_{\text{signal}}}{\sqrt{\text{gain}_{\text{background}}}}. \tag{5.1}$$

Equation (5.1) is an estimate which assumes that the background analysis will not improve to reject the increased background acceptance from the OR'd triggers. This may not be true for adaptive analysis techniques such as boosted decision trees or neural network analyses. Two Monte-Carlo samples are used for the tb and tqb channels: a tb-like background $t\bar{t} \rightarrow l + \nu + 2b$ with 283463 events, and a tqb-like background $t\bar{t} + q \rightarrow l + \nu + 2b + q$ with 98425 events, which were reduced from the pre-selection cuts to 42481 and 14501 events respectively. The tb-like and tqb-like background trigger efficiencies were, for the combined v8-v14 trigger lists, 90.1% (tb-like) and 90.6% (tqb-like) for the original e+Jets triggers, and 93.2% (tb-like) and 93.6% (tqb-like) for the $E_S \vee EJ$ triggers. This is a gain of 3.1% for the tb-like and 3.0% for the tqb-like, $t\bar{t}$ events.

The estimated signal significance for the tb and tqb channels give an increase of 4.7% and 5.7% over the $t\bar{t}$ background considered. A more accurate estimate of the signal significance would require the entire analysis chain to be run, which is prohibitively difficult. This must be done in order for the adaptive techniques of the boosted decision trees or neural networks used in the analyses to use the events from the increased acceptance of the signal and the background.

caf_trigger was written in a form which allows for the compartmentalization of the different triggers that were used to create the combined OR'd triggers. This enables us to determine the benefit of the e+Jets OR'd triggers over the original e+Jets triggers without the single electron triggers added in. The individual trigger lists were performed with v12-v14 since there was only a single e+Jets trigger term for v8-v11, and the full set of trigger lists and luminosities were used for the

luminosity averaged efficiency. It is interesting to note that an OR of the e+Jets trigger brings at least 2 additional terms to the main e+Jets trigger: a CEM(2, 6) L1 term, and a CEM(2, 3)CEM(1, 9) L1 term, where additional terms result in a change in the L2 condition (Table (4.3) and (4.4)). The luminosity averaged trigger efficiencies, were calculated for the v8-v14 trigger lists: $83.6\pm^{0.6}_{0.5}\%$ for *tb* MC and $82.2\pm^{0.6}_{0.6}\%$ for *tqb* MC for the original e+Jets trigger and $84.1\pm^{0.6}_{0.5}\%$ *tb* MC and $82.7\pm^{0.6}_{0.6}\%$ *tqb* MC for the OR'd e+Jets triggers which is a gain of 0.5% for *tb* MC and 0.5% for *tqb* MC. The uncertainties were produced through the sigma calculations available in *caf_trigger* for the averaged efficiencies of the v8-v14 trigger lists. The probability distribution for all the trigger lists is shown in Figure (5.2), and the efficiencies for the individual trigger list for the *tb* and *tqb* MC are shown in Table (5.1). A representative example can be seen between the v12 and v14 e+Jets triggers. Both of these triggers add only the two L1 terms listed above and they both show a negligible gain in the overall efficiency of the triggers. The gains in efficiency, for the *tqb* MC events, are from 81.3% to 81.5% for v12, and from 81.1% to 81.8% for v14 or an overall gain of 0.2% and 0.7% respectively (Figure (5.1)).

The small gain is not unexpected as the only changes in the trigger are made at L1 and only to the number and energy of the electrons. The gain in efficiency is less than the uncertainty in the trigger efficiencies which indicates that the OR of the various e+Jets does not contribute to a useful improvement in the efficiency. As a comparison, the gain of the acceptance of the *tb*-like, and *tqb*-like $t\bar{t}$ backgrounds was calculated. This was done to see if the e+Jets OR'd triggers accepted more background events than the original e+Jets triggers. The luminosity averaged trigger efficiencies of the backgrounds for the v8-v14 trigger lists are: $90.1\pm^{0.9}_{14.3}\%$ *tb*-like and $90.6\pm^{0.}_{0.}\%$ *tqb*-like for the original e+Jets triggers, and $90.8\pm^{0.9}_{14.3}\%$ *tb*-like and $91.3\pm^{0.}_{0.}\%$ *tqb*-like for the e+Jets OR'd triggers.

The gain in the acceptance of the background events is consistent with zero, which is the same result as was found for the signal events. This means that the use of the e+Jets OR'd triggers does not contribute negatively to the overall signal

Table 5.1: e+Jets ORs vs original e+Jets trigger efficiencies, for the leading electron, of the *tb*-eνbb and *tqb*-eνbqb MC vs trigger list. Trigger lists v8-v11 have been combined since there are no changes to the triggers during that period.

Trigger List	v8-v11	v12	v13.0	v13.3	v14
tb e+Jets ORs	89.9%	83.1%	84.2%	83.5%	83.3%
tb e+Jets original	89.9%	82.8%	83.5%	82.8%	82.6%
tqb e+Jets ORs	89.4%	81.5%	82.6%	81.6%	81.8%
tqb e+Jets original	89.4%	81.3%	82.0%	81.0%	81.1%

significance, which does not change the results of the study for the ORing with the single electron triggers. The e+Jets OR'd triggers should not be used in the future as they do not contribute to the increase in the signal significance while adding appreciable overhead to the calculation.

The trigger turn-on curves produced in *em_cert* were not fitted to an error function which precludes the advantage of the fitted curve smoothing out any statistical fluctuations. This was due to the turn-on curves being an OR of many single turn-on curves which causes an error function fit to incorrectly represent the data points. This can be mediated in the future by fitting the single turn-on curves with an error function. These can then be used as a first approximation for a fit of the OR'd turn-on curve with the sum of several error functions.

The triggers studied have L3 conditions that require an electron or jet to have a p_T greater than a specified threshold. An additional requirement can be added for a particle track to have a p_T threshold as well. The addition of a track requirement improves the chance that an object identified as an electron will have a matching track. The ability to trigger on tracks was not implemented in *em_cert* at the time of this study and so could not be tested.

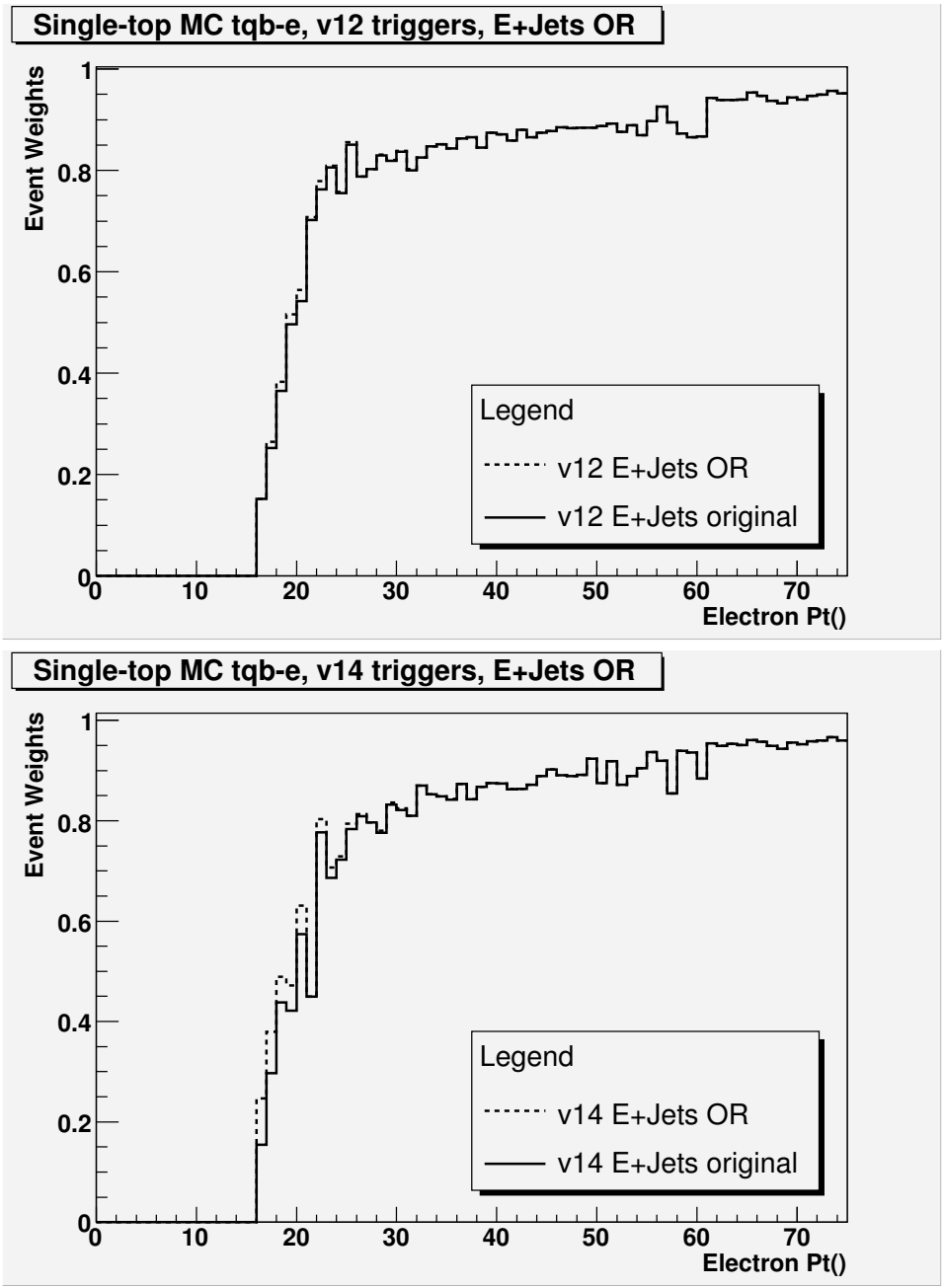

Figure 5.1: e+Jets ORs vs original e+Jets trigger probability distribution in p_T for the leading electron. Top: trigger list v12, tqb-eνbqb MC. Bottom: trigger list v14, tqb-eνbqb MC.

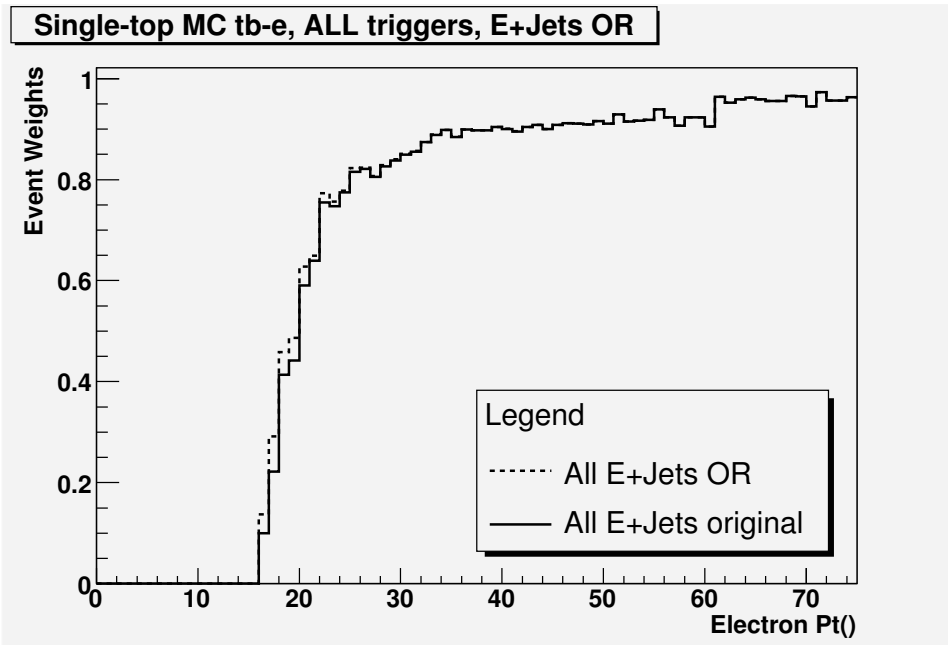

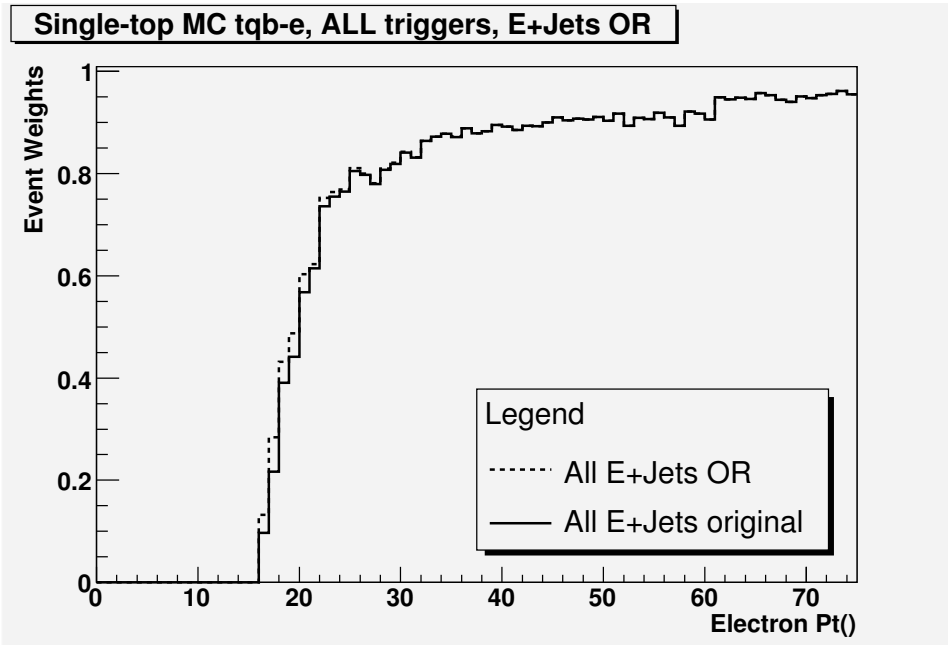

Figure 5.2: e+Jets ORs vs original e+Jets trigger probability distribution in p_T for the leading electron.

Bibliography

[1] T. LeCompte, H. T. Diehl, "The CDF and D0 Upgrades for Run II," *Annual Review of Nuclear and Particle Science*, Vol. 50, p71-177, December 2000.

[2] L. de Broglie, "Ondes et Quanta/Waves and Quanta," *Comptes Rendus, 117, 507, 548, 630 (1923)*, 1984.

[3] . Gell-Mann, "The Eightfold Way: A Theory of Strong Interaction Symmetry," *California Institute of Technology Report CTSL-20, 1961 unpublished*, reprinted in The Eightfold Way, 1964.

[4] P. W. Higgs, "Broken symmetries, massless particlees and gauge fields," *Physical Letters, Volume 12, Issue 2, p. 132-133*, September 1964.

[5] The SNO Collaboration, "Direct Evidence for Neutrino Flavor Tranformation from Neutral-Current Interactions in the Sudbury Neutrino Observatory," *Phys. Rev. Lett. Volume 89, No. 1, 011302 (2002)* .

[6] P. A. M. Dirac, "A Theory of Electrons and Protons," *Proc. Roy. Soc. A***126,** 360 (1930).

[7] Kobayashi, M.; Maskawa, T., "CP-Violation in the Renormalizable Theory of Weak Interaction," *Progr. of Theor. Phys.* **49,** 652 (1973).

[8] CDF Collaboration, "Observation of the Top Quark," *Phys. Rev. Lett.* **74,** 2626 (1995).

[9] D0 Collaboration, "Observation of the Top Quark," *Phys. Rev. Lett.* **74,** 2632 (1995).

[10] Tevatron Electroweak Working Group (for the CDF and D0 Collaborations), "Combination of CDF and DO Results on the Mass of the Top Quark," *hep-ex/0608032, Aug 2006* .

[11] M. Cacciari, S. Frixione, M.L. Mangano, P. Nason, G. Ridolfi, "The t Anti-t Cross Section at 1.8-TeV and 1.96-TeV," *J. High Energy Phys.* **0404**, :068, 2004, hep-ph/0303085, March 2003.

[12] The BABAR Collaboration, "Observation of CP violation in the B^0 meson system," *SLAC-PUB-8904*, hep-ex/0107013, July 2001.

[13] I. Bigi, Y. Dokshitzer, V. Khoze, J. Kühn, and P. Zerwas, "Production and Decay Properties of Ultra-Heavy Quarks," *Phys. Lett. B***181,**, 157 (1986).

[14] M. Jezabek, and J. Kühn, "V-A Tests Through Leptons from Polarized Top Quarks," *Phys. Lett. B***329,**, 317 (1994).

[15] Francis Halzen, Alan D. Martin, "Quarks & Leptons: An Introductory Course in Modern Particle Physics," *John Wiley & Sons Inc.*, 1984.

[16] Particle Data Group, "Review of Particle Physics," *Journal of Physics G, Nuclear and Particle Physics*, Vol. 33, July 2006.

[17] T. Tait and C.-P. Yuan, "Single Top Quark Production as a Window to Physics Beyond the Standard Model," *Phys. Rev. D* **63,** 014018 (2001), hep-ph/0007298, 17 Oct 2000.

[18] D0 Collaboration, "The Upgraded D0 Detector," *Preprint submitted to Elsevier Preprint* .

[19] Department of Energy Review Committee, "Report on the Technical, Cost, Schedule and Management Review of the TEVATRON Run II Luminosity Upgrades, February 2004," *Department of Energy* .

[20] D0 Experiment, "D0 Detector Pictures,"
URL: http://www-d0.fnal.gov/Run2Physics/WWW/drawings.htm.

[21] B. Vachon, et. al, "Top Trigger Efficiency Measurements and the top_trigger package," *D0 Note 4512*, July 2004.

[22] Rene Brun, Fons Rademakers, "ROOT - An Object Oriented Data Analysis Framework," *Preprint submitted to Elsevier Preprint*, May 1997.

[23] Z. Sullivan, "Understanding Single-Top-Quark Production and Jets at Hadron Colliders," *Phys. Rev. D* **70,** 114012 (2004), hep-ph/0408049, 25 Oct 2004.

[24] J.Hays, J.Mitrevski, C.Schwanenberger, "The Program Package em_cert: Version p18-br-20," *D0 Note 5070*, March 2006.

[25] Camille Belanger-Champagne, "trigeff_cafe: Single Object Efficiency Calculation in the CAFe Environment," *D0 Note 5093*, May 2006.

[26] Axel Naumann and Frank Filthaut, "Combining Prescaled Triggers," *D0 Note 4844*, June 2005.

[27] Configuration Files, "Skim definitions for 2EMhighPT and TOP-JETTRIG," *http://www-d0.fnal.gov/Run2Physics/cs/skimming/ + skim_p17.07.01/np_tmb_stream/rcp/2EMhighpt_stream.rcp*, *http://www-d0.fnal.gov/Run2Physics/cs/skimming/ + skim_p17.07.01/np_tmb_stream/rcp/TOP_JET_TRIG_stream.rcp*, June 2005.

[28] Torbjörn Sjöstrand, Stephen Mrenna, and Peter Skands, "The complete PYTHIA 6.400 manual," *JHEP 05, 026 (2006)* LU TP 06-13, FERMILAB-PUB-06-052-CD-T, hep-ph/0603175, March 2006.

[29] R. Brun, *et al.*, "CERN Program Library Writeup W5013," *(1993)* .

[30] A. Pukhov *et al.*, "Report INP-MSU 98-41/542," hep-ph/9908288; http://theory.sinp.msu.ru/comphep.

[31] E. Boos, L. Dudko, V. Savrin, and A. Sherstnev, "in preparation; E. Boos, L. Dudko, and V. Savrin," *CMS Note 2000/065* .

[32] D. J. Lange, "The Evtgen Particle Decay Simulation Package," *Nucl. Instrum. Meth. A* **462,** 152 (2001).

[33] M. Begel *et al.*, "DØ Luminosity in Run 2: Delivered, Triggered and Recorded," *DØ Note 3970, 3971 and 3972,*

Appendix A: *em_cert* turn-on curves

These are the turn-on curves produced in *em_cert* for E_S, E_{EJ}, $E_S \wedge E_{EJ}$, $E_{EJ} \wedge SCJET$, and $E_S \wedge E_{EJ} \wedge SCJET$ for trigger lists v8-v14.

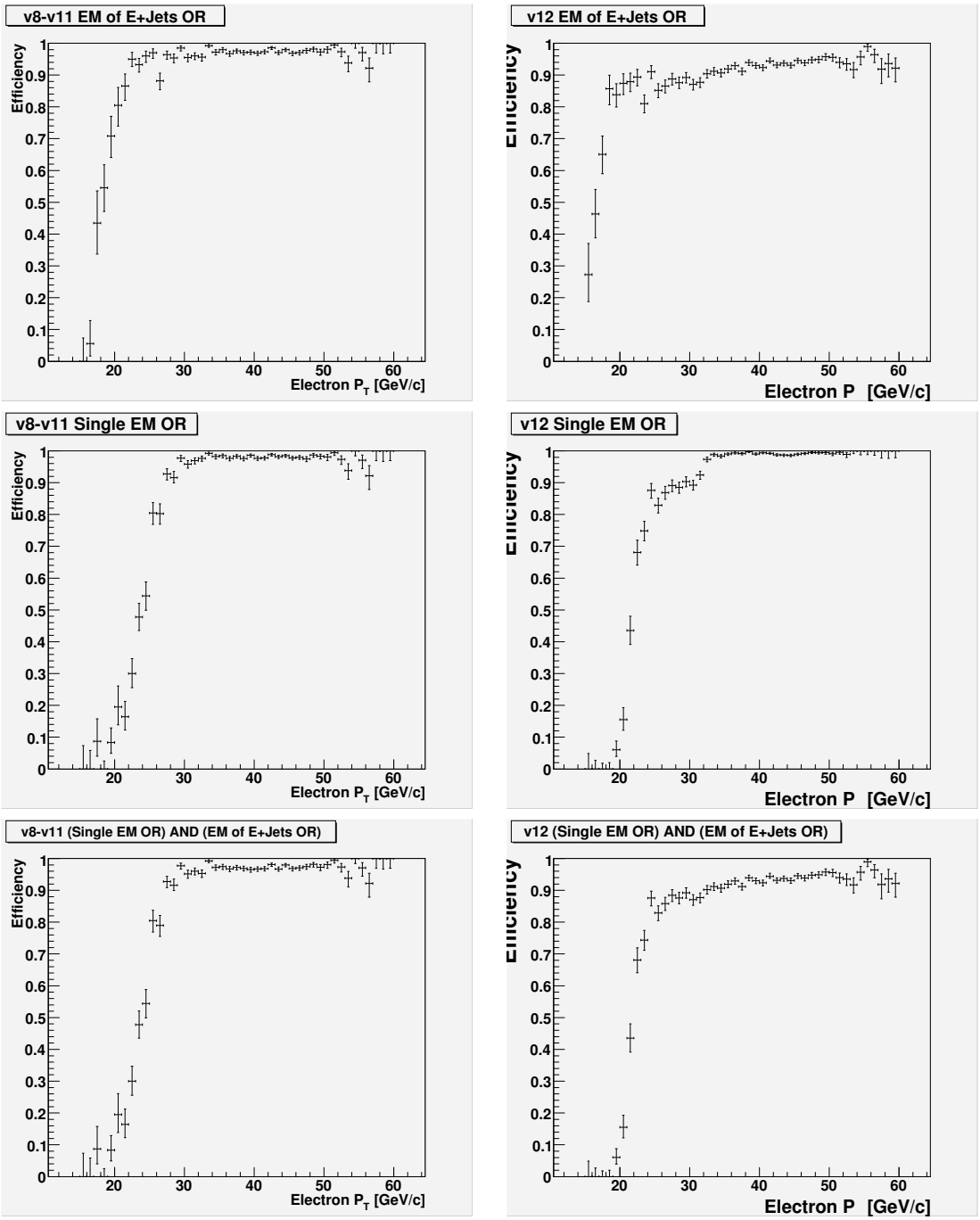

$v8 - v11$ $v12$

Figure 5.3: Turn-on curves for E_S, E_{EJ} and $E_S \wedge E_{EJ}$ for trigger lists v8-v12.

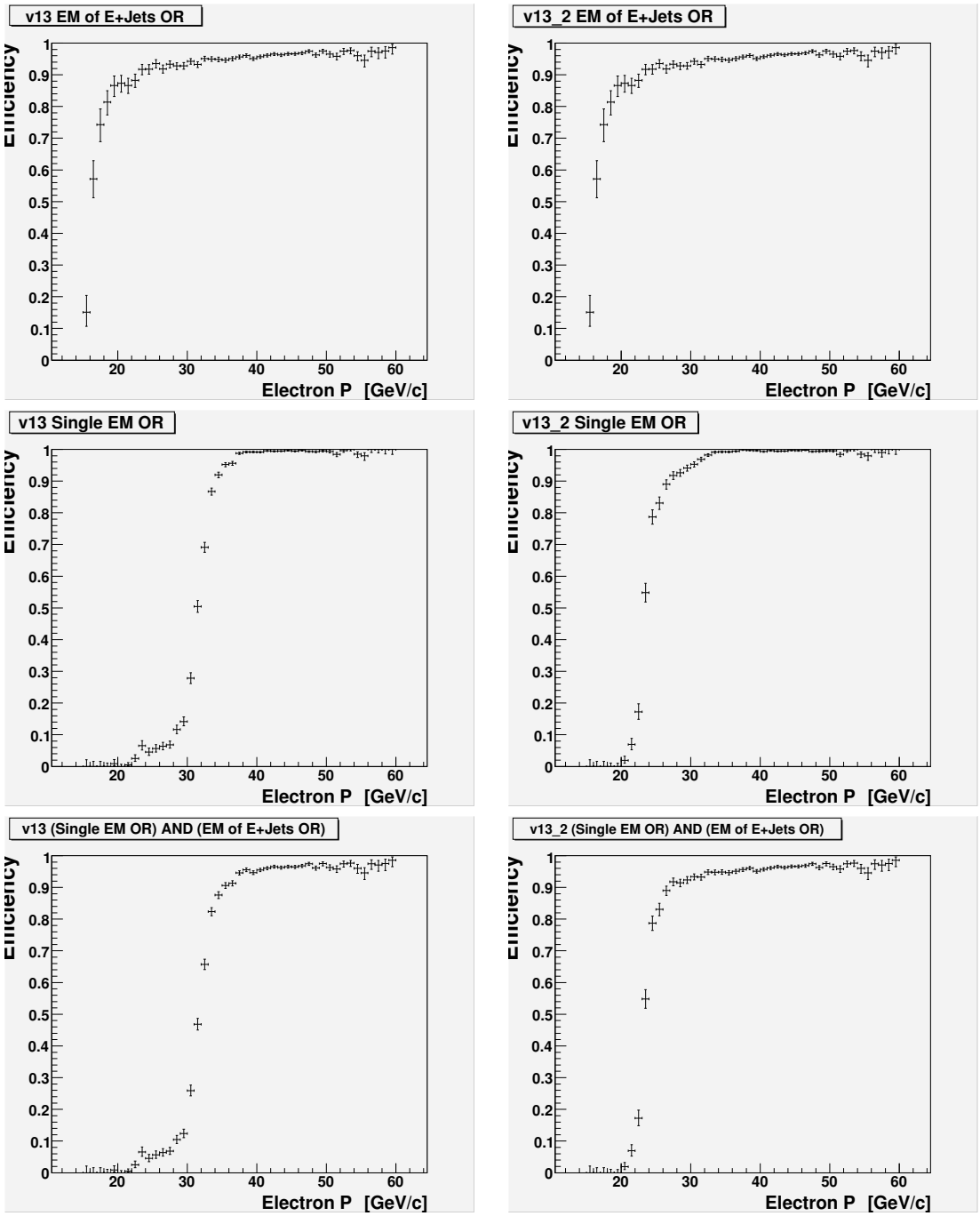

$v13$ $v13.2$

Figure 5.4: Turn-on curves for E_S, E_{EJ} and $E_S \wedge E_{EJ}$ for trigger lists v3-v13.2.

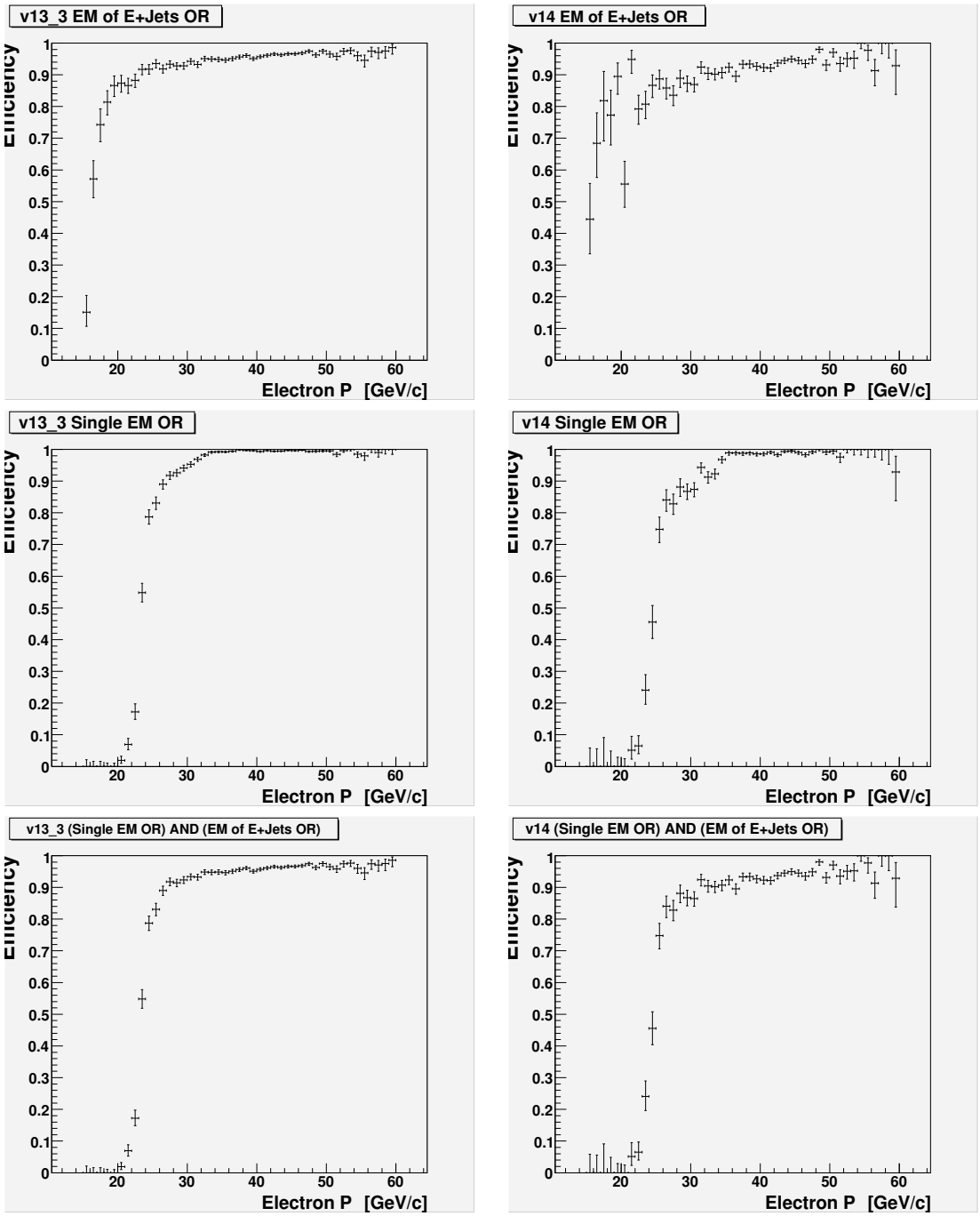

$v13.2$ $v14$

Figure 5.5: Turn-on curves for E_S, E_{EJ} and $E_S \wedge E_{EJ}$ for trigger lists v13.2-v14.

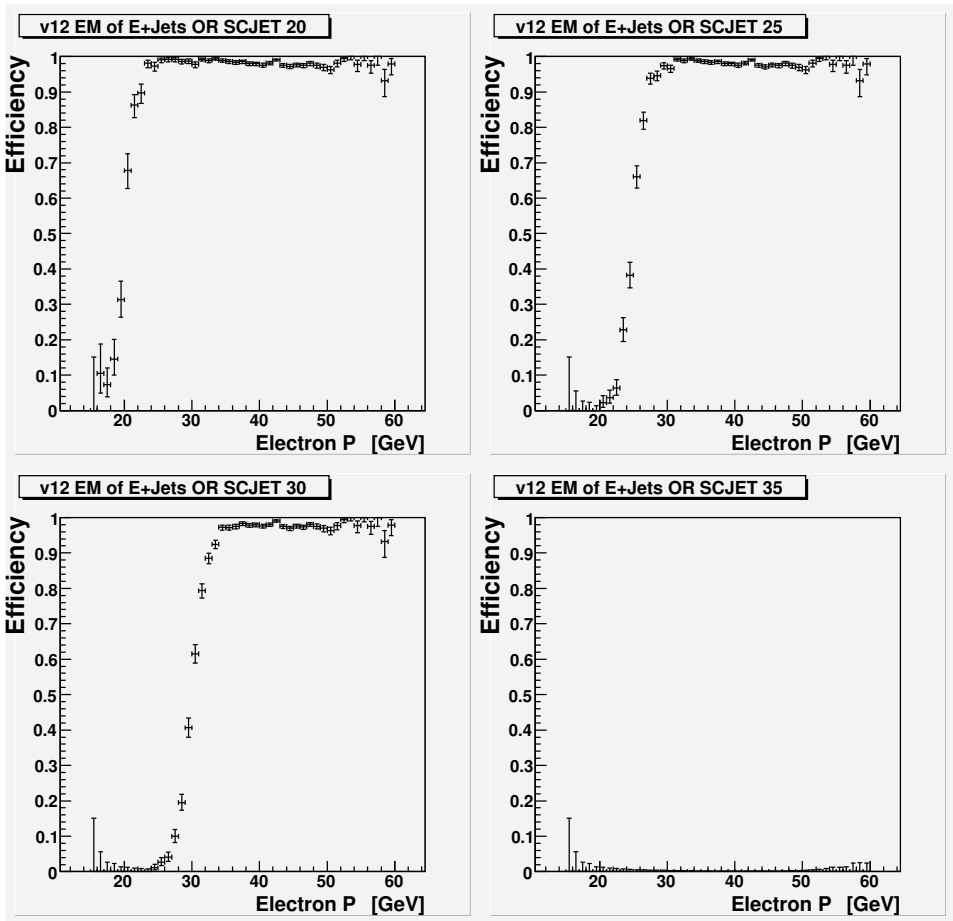

Figure 5.6: The turn-on curve for the v12 electron triggers firing a jet trigger: $Ex_SHT15 \wedge SCJET(y)$, where x = 1, 2, 3 and y = p_T threshold of 20, 25, 30 and 35 GeV.

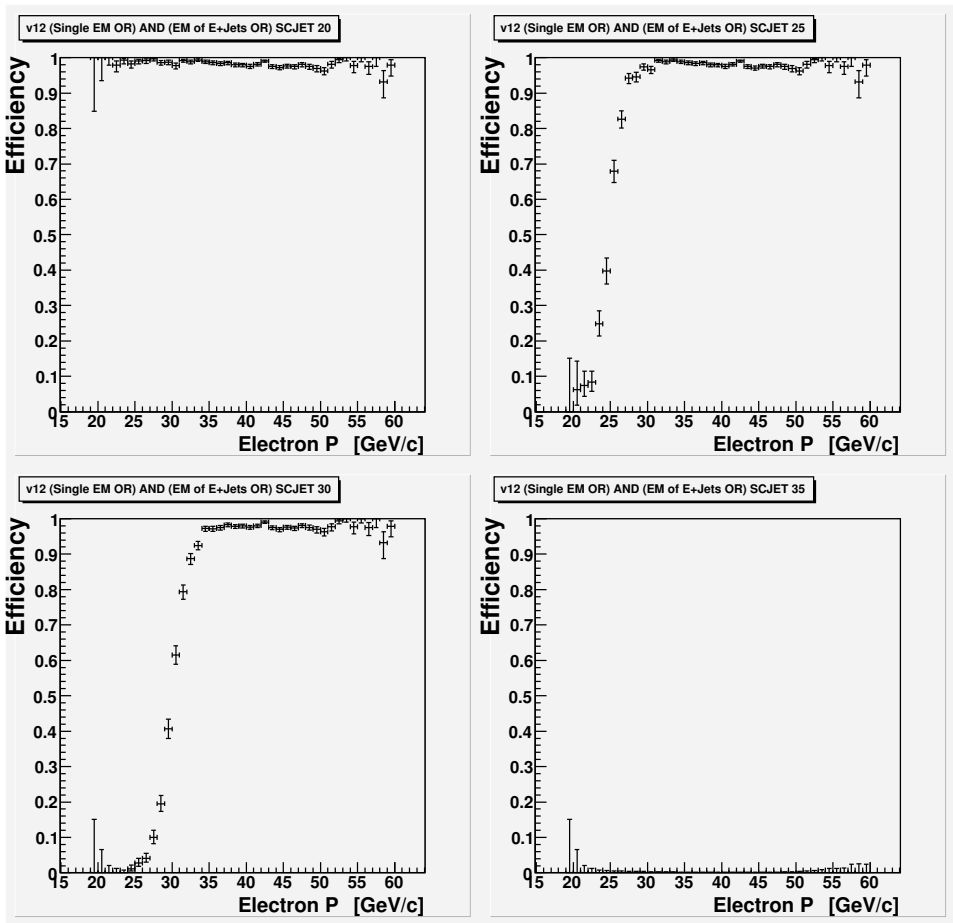

Figure 5.7: The turn-on curve for the v12 electron triggers firing a jet trigger: $(Ex_SHT20 \vee Ex_SH30 \vee E1_L50 \vee E1_VL70) \wedge Ex_SHT15 \wedge SCJET(y)$, where x = 1, 2, 3 and y = p_T threshold of 20, 25, 30 and 35 GeV.

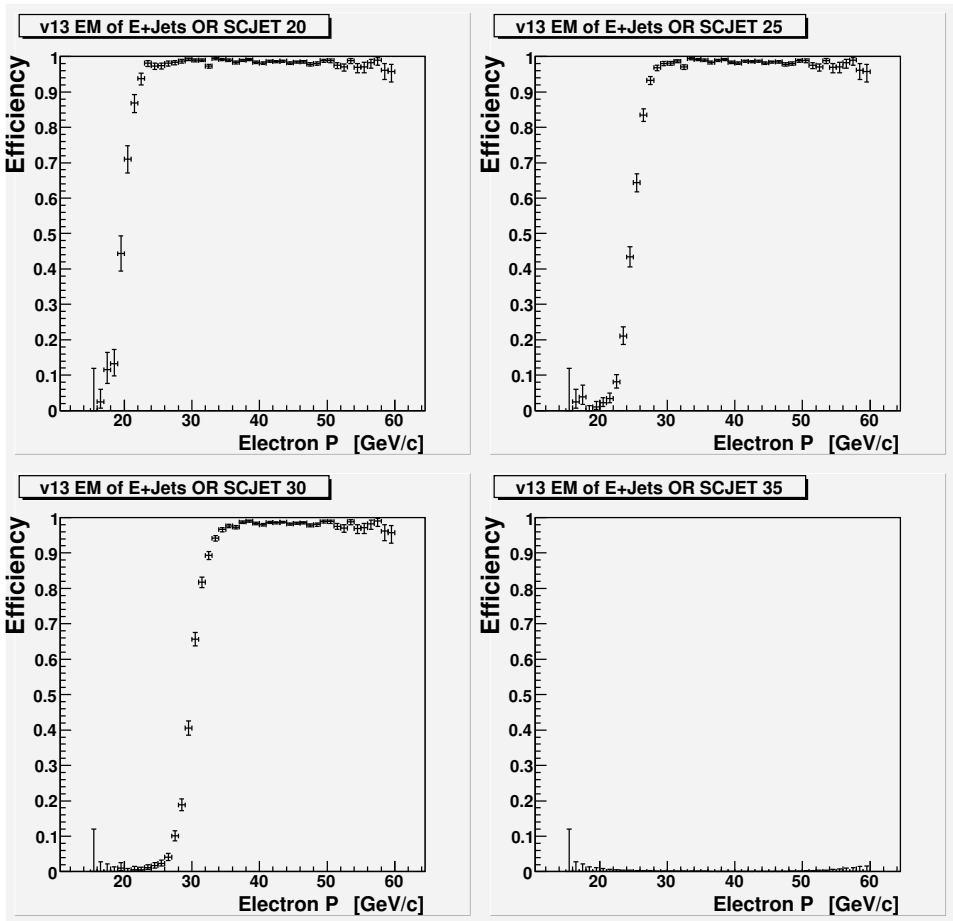

Figure 5.8: The turn-on curve for the v13 electron triggers firing a jet trigger: $Ex_SHT15 \wedge SCJET(y)$, where x = 1, 2, 3, 4 and y = p_T threshold of 20, 25, 30 and 35 GeV.

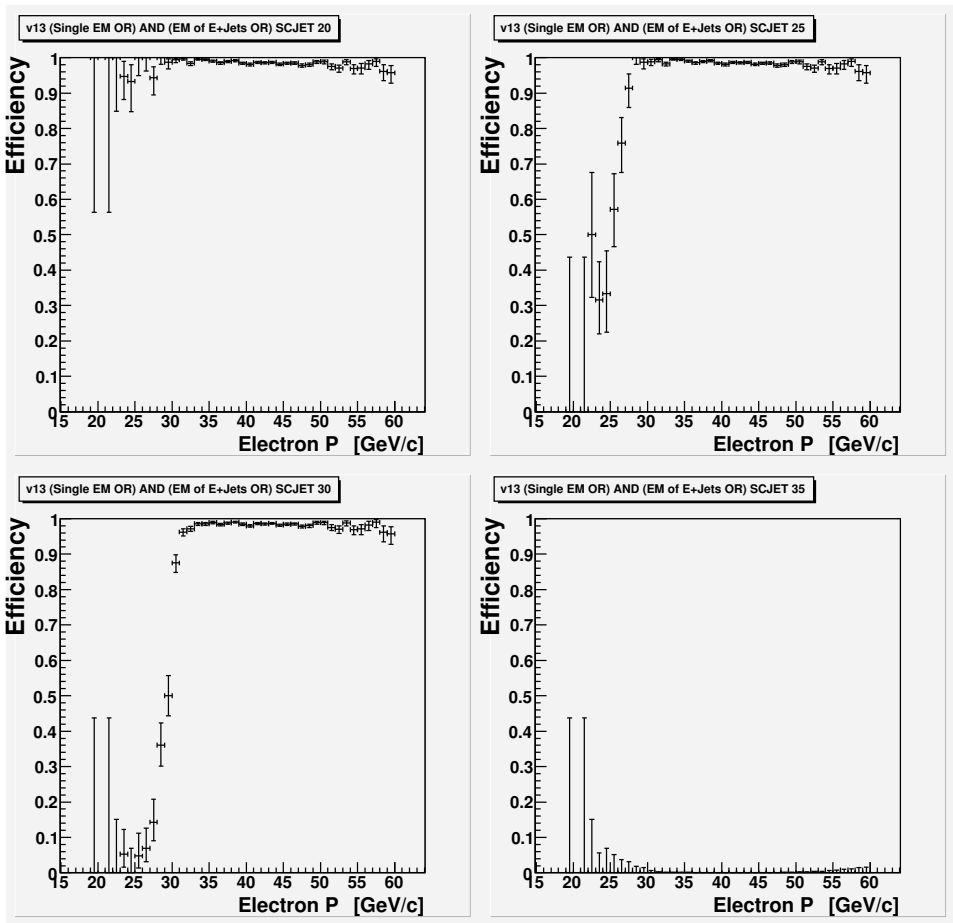

Figure 5.9: The turn-on curve for the v13 electron triggers firing a jet trigger: $(Ex_SHT20 \vee Ex_SH30 \vee E1_L50 \vee E1_NC90) \wedge Ex_SHT15 \wedge SCJET(y)$, where x = 1, 2, 3, 4 and y = p_T threshold of 20, 25, 30 and 35 GeV.

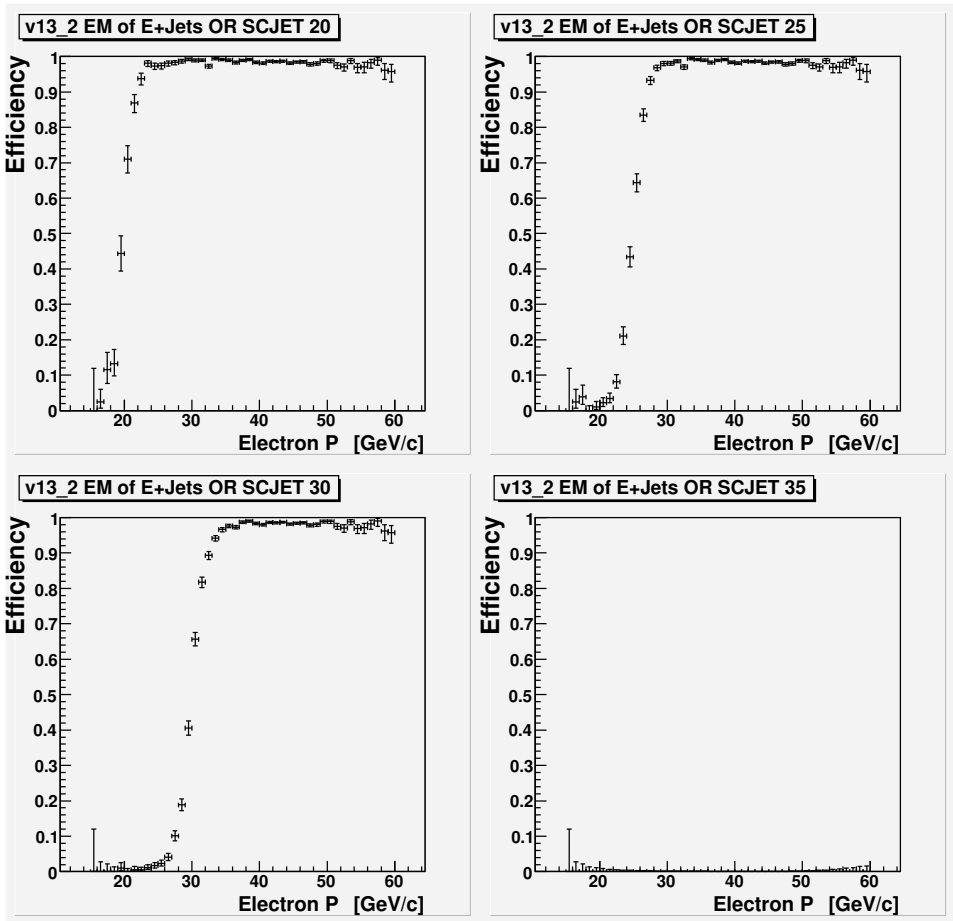

Figure 5.10: The turn-on curve for the v13.2 electron triggers firing a jet trigger: $Ex_SHT15 \wedge SCJET(y)$, where x = 1, 2, 3, 4 and y = p_T threshold of 20, 25, 30 and 35 GeV.

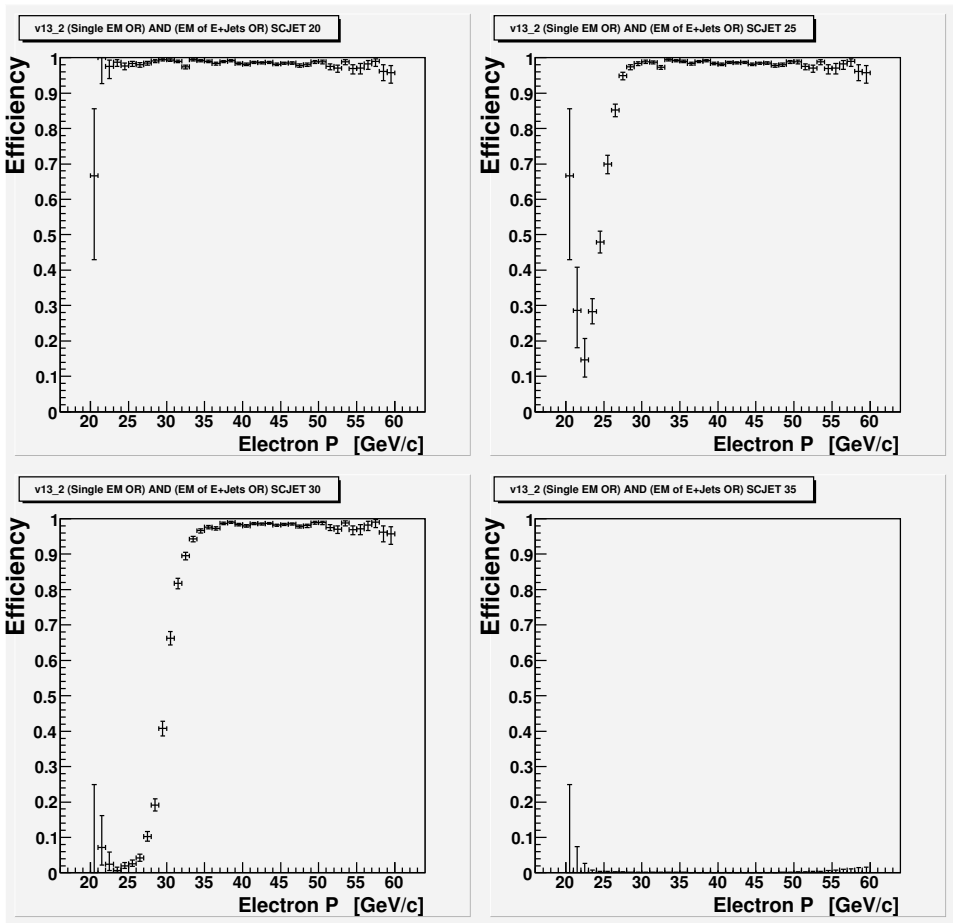

Figure 5.11: The turn-on curve for the v13.2 electron triggers firing a jet trigger: $(Ex_SHT22 \vee Ex_SH30 \vee E1_L70 \vee E1_NC90) \wedge Ex_SHT15 \wedge SCJET(y)$, where x = 1, 2, 3, 4 and y = p_T threshold of 20, 25, 30 and 35 GeV.

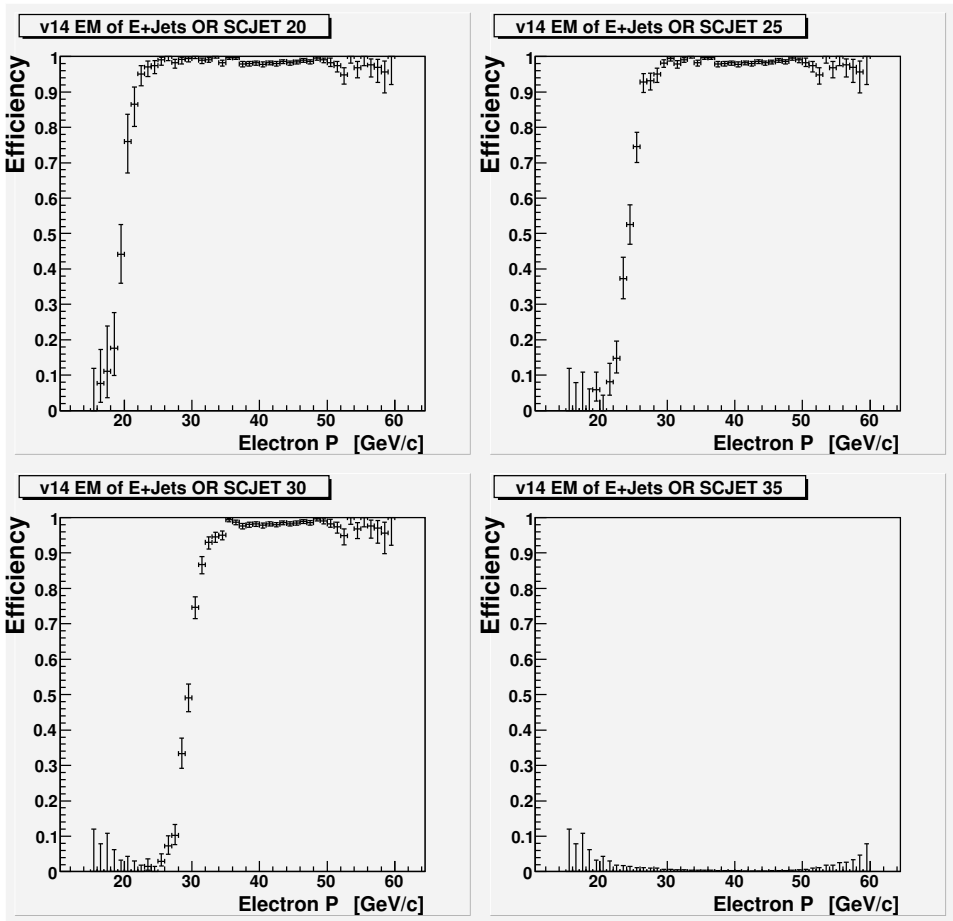

Figure 5.12: The turn-on curve for the v14 electron triggers firing a jet trigger: $Ex_SHT15 \wedge SCJET(y)$, where x = 1, 3, 4 and y = p_T threshold of 20, 25, 30 and 35 GeV.

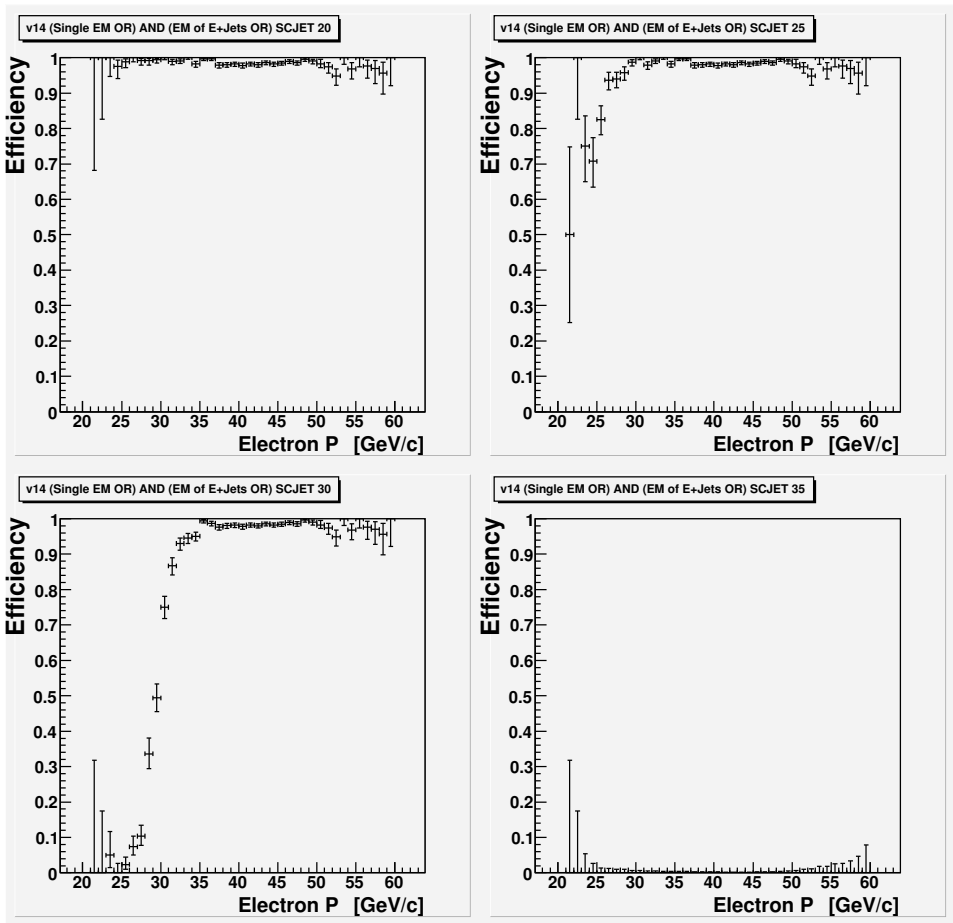

Figure 5.13: The turn-on curve for the v14 electron triggers firing a jet trigger: $(Ex_SHT25 \vee Ex_SH35 \vee E1_L70) \wedge Ex_SHT15 \wedge SCJET(y)$, where x = 1, 3, 4 and y = p_T threshold of 20, 25, 30 and 35 GeV.

Appendix B: *caf_trigger* trigger efficiency curves

These are the trigger efficiency curves produced in *caf_trigger*, from the turn-on curves produced in *em_cert*, for the original E+Jets triggers in comparison with the $E_S \vee EJ$ triggers for trigger lists v8-v14.

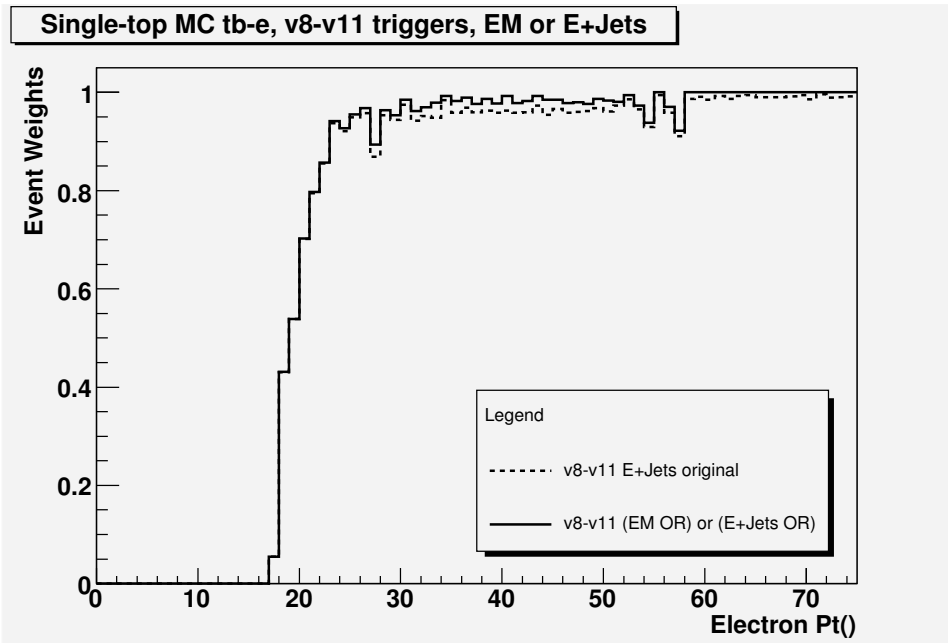

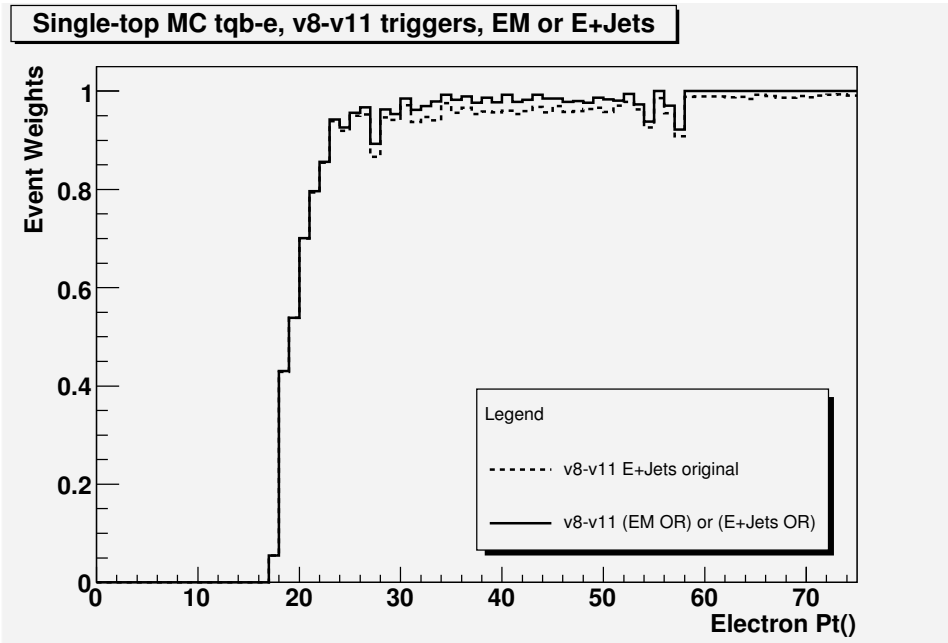

Figure 5.14: Trigger list v8-v11: $E_S \vee EJ$ vs original E+Jets trigger probability distribution in p_T for the leading electron.

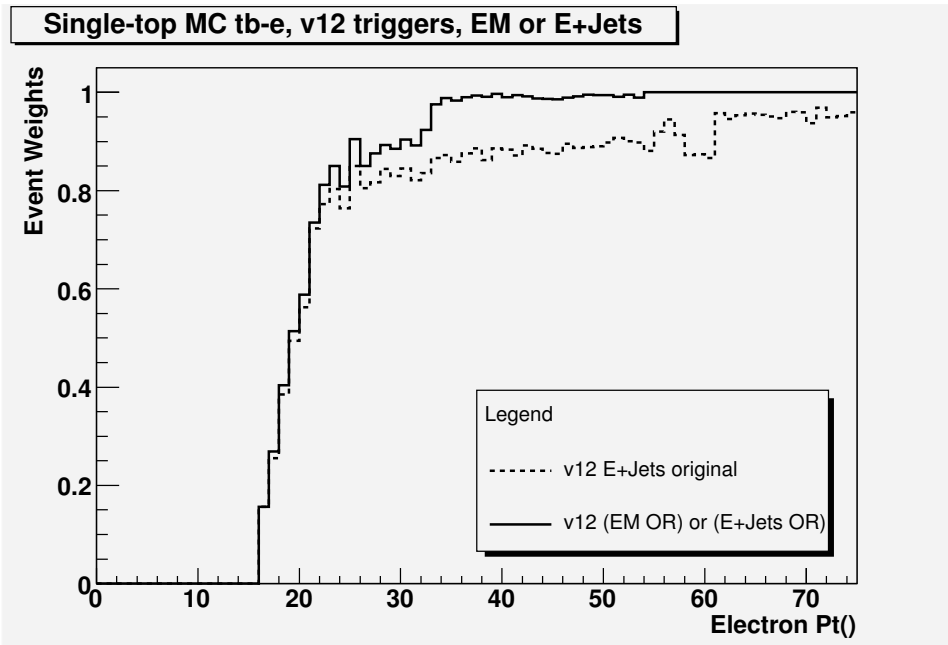

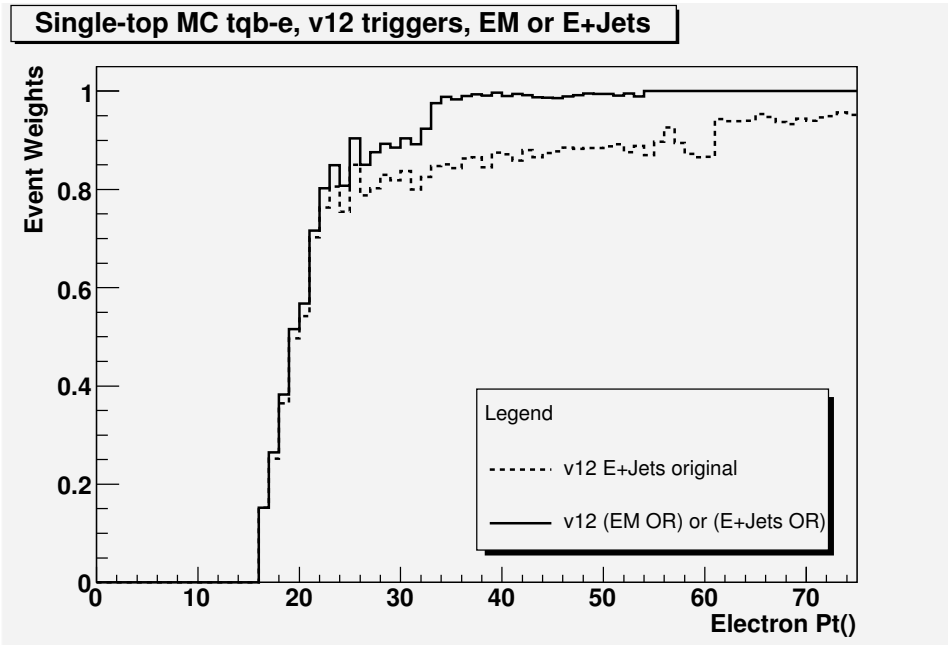

Figure 5.15: Trigger list v12: $E_S \vee EJ$ vs original E+Jets trigger probability distribution in p_T for the leading electron.

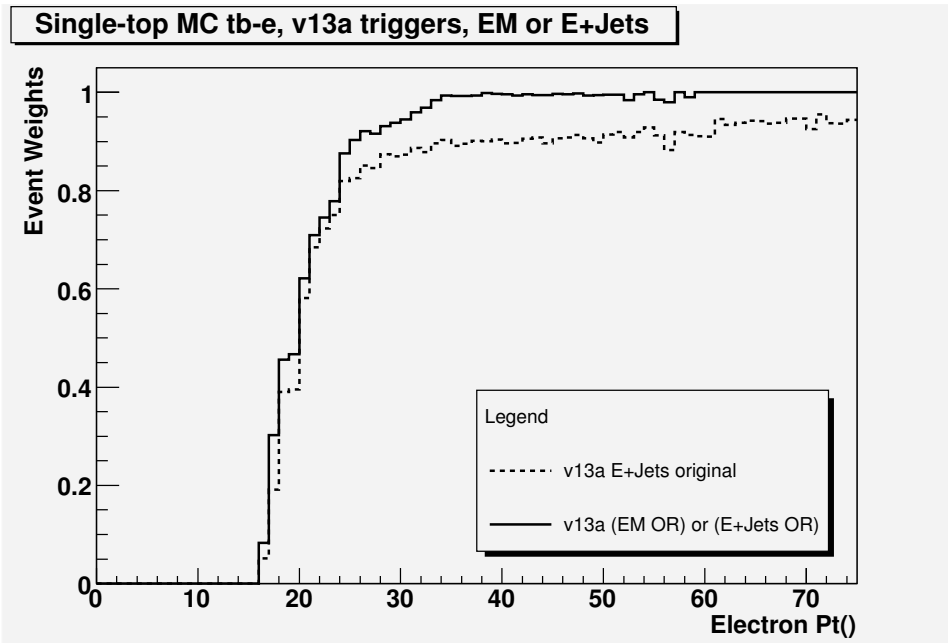

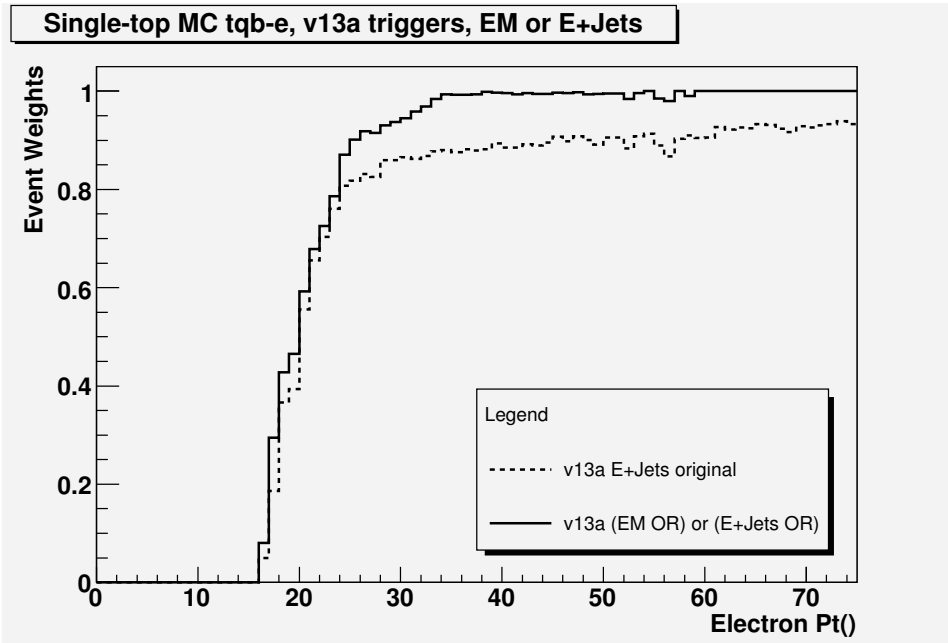

Figure 5.16: Trigger list v13a: $E_S \vee EJ$ vs original E+Jets trigger probability distribution in p_T for the leading electron.

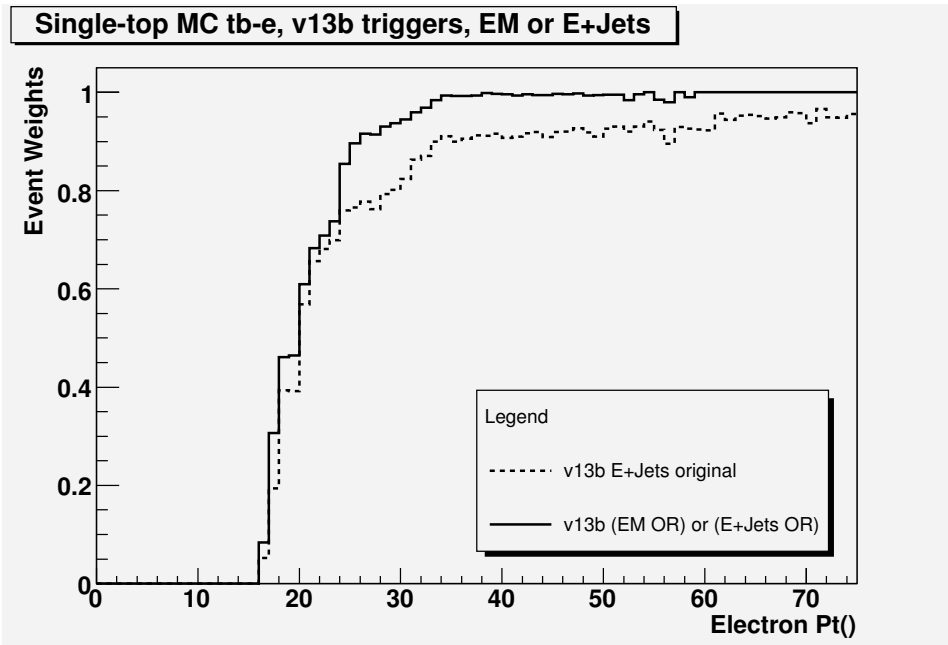

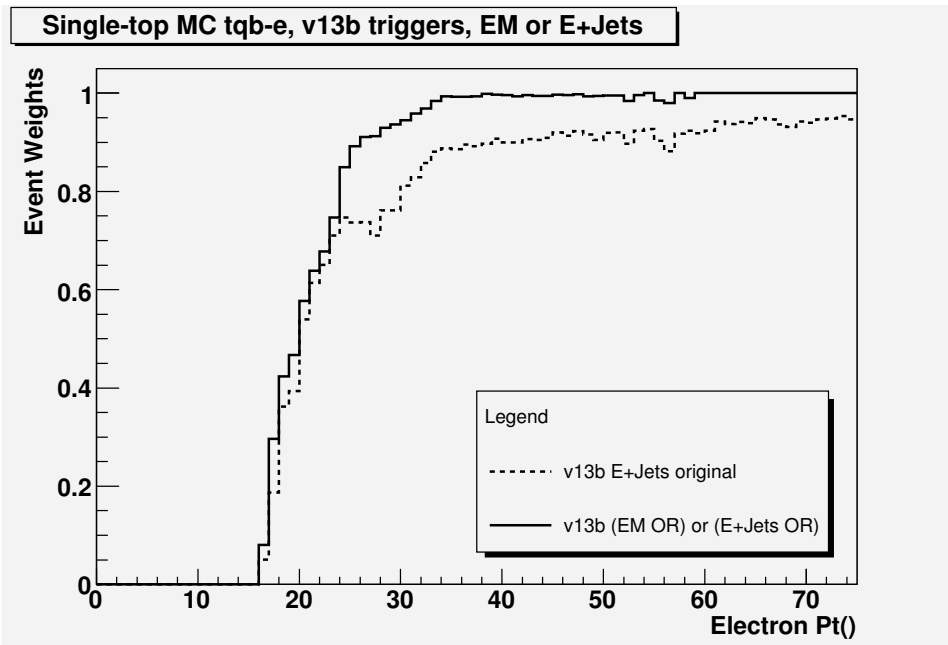

Figure 5.17: Trigger list v13b: $E_S \vee EJ$ vs original E+Jets trigger probability distribution in p_T for the leading electron.

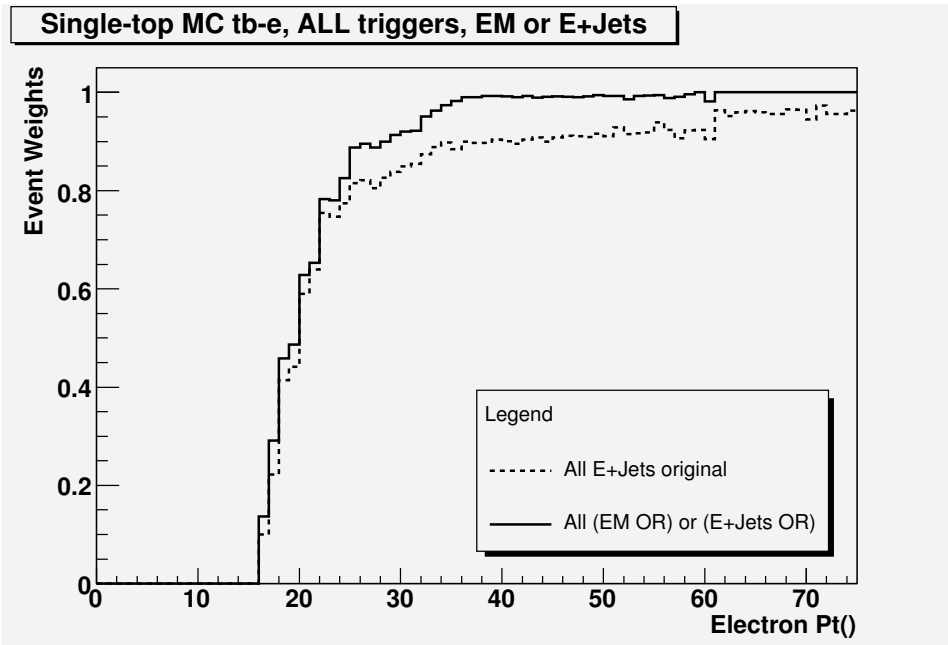

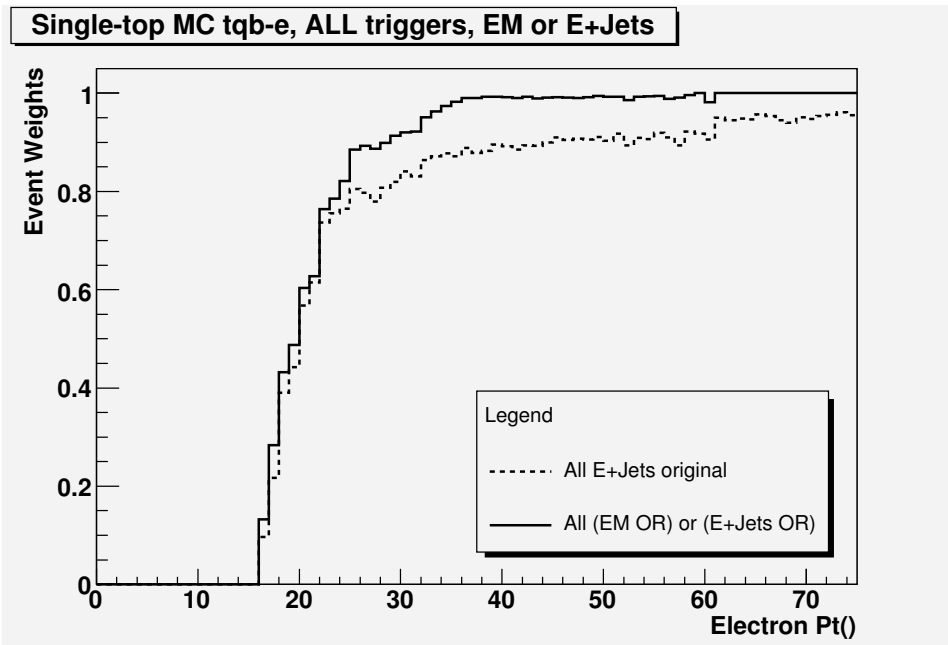

Figure 5.18: Trigger list v14: $E_S \vee EJ$ vs original E+Jets trigger probability distribution in p_T for the leading electron.